

# 13 Small-Angle Neutron Scattering and Applications in Soft Condensed Matter

I. GRILLO

<b>1</b>	<b><i>Introduction</i></b>	<b>707</b>
<b>2</b>	<b><i>Description of SANS Instruments</i></b>	<b>707</b>
2.1	The Steady-State Instrument D22	708
2.2	The Time-of-Flight Instrument LOQ	709
2.3	Detectors for SANS Instruments	711
2.4	Sample Environments	713
<b>3</b>	<b><i>Course of a SANS Experiment</i></b>	<b>713</b>
3.1	Definition of the q-Vector	713
3.2	Choice of Configurations and Systematic Required Measurements	714
3.2.1	Collimation	715
3.2.2	Beam Center Determination	715
3.2.3	Beam-Stop Alignment	715
3.2.4	Electronic Background	716
3.2.5	Standard for Calibration	716
3.2.6	Transmission	716
3.2.7	Counting Time	717
3.2.8	Command Files	717
3.3	Conclusion	717
<b>4</b>	<b><i>From Raw Data to Absolute Scaling</i></b>	<b>718</b>
4.1	Determination of the Incident Flux $\Phi_0$	719
4.2	Normalization with a Standard Sample	719
4.3	Solid Angle $\Delta\Omega(Q)$	721
4.4	Transmission	722
4.4.1	Definition	722
4.4.2	Numerical Applications and Examples	723
4.4.3	Transmission at Large Angles	724
4.5	Multiple Scattering	725
4.5.1	Transmission at Large Angles	726
4.5.2	How to Prevent Multiple Scattering?	727

4.6	Subtraction of Incoherent Background .....	727
4.7	Conclusion .....	728
<b>5</b>	<b><i>Modeling of the Scattered Intensity</i> .....</b>	<b>728</b>
5.1	Rules of Thumb in Small-Angle Scattering .....	728
5.2	SLD, Contrast Variation, and Isotopic Labeling .....	731
5.2.1	The Zero Average Contrast Method .....	732
5.2.2	Contrast Variation Technique .....	733
5.2.3	Contrast and Background .....	734
5.2.4	Limits of Isotopic Labeling .....	734
5.3	Analytical Expressions of Particle Form Factors .....	735
5.3.1	Sphere .....	736
5.3.2	Concentric Shells and Hollow Sphere .....	736
5.3.3	Cylinder .....	737
5.3.4	Ellipsoid .....	737
5.3.5	The Guinier Approximation .....	738
5.3.6	The Zimm Approximation .....	738
5.3.7	Fractals .....	738
5.3.8	Concentrated Surfactant Phases .....	739
5.3.9	Case of Polymers .....	740
5.3.10	Case of Interfaces .....	740
5.4	Indirect Fourier Transform Method .....	741
5.5	Structure Factors of Colloids .....	743
<b>6</b>	<b><i>Instrument Resolution and Polydispersity</i> .....</b>	<b>745</b>
6.1	Effect of the Beam Divergence and Size: $\theta$ Resolution .....	747
6.2	Effect of the $\lambda$ Distribution .....	747
6.3	Smearing Examples .....	749
6.3.1	Evidence of Wavelength Spread on Bragg Peaks .....	749
6.3.2	Importance of the Choice of Instrument Configurations .....	750
6.4	Polydispersity .....	751
6.5	Instrumental Resolution and Polydispersity .....	752
6.6	Conclusion .....	753
6.7	Appendix: Definition of $\Delta\theta$ and $\Delta\lambda/\lambda$ ; Comparison between Triangle and Gaussian Functions .....	754
6.7.1	Wavelength Distribution .....	754
6.7.2	Angular Distribution .....	755
<b>7</b>	<b><i>Present Future and Perspective</i> .....</b>	<b>756</b>
7.1	Recent Developments .....	756
7.2	Future Developments .....	757
7.2.1	Interactive Instrument Control .....	757
7.2.2	Lenses and Focusing .....	758
7.2.3	Ultra Small-Angle Scattering (USANS) .....	758
7.2.4	Polarization and SANS .....	759
7.3	General Conclusion .....	759

## 1 Introduction

The aim of a small-angle neutron scattering (SANS) experiment is to determine the shape and the organization, averaged in time, of particles or aggregates dispersed in a continuous medium. The term particle is applied to a wide range of objects, as for example, small colloidal particles (clay, ferrofluid, nanotube), surfactant aggregates (micelles, lamellar, hexagonal, cubic, or sponge phases), polymers and all derivatives, liquid crystal, model membranes, proteins in solution, flux line lattices in supraconductors. The list is not exhaustive.

Small-angle scattering was discovered in the late 1930s by Guinier during X-ray diffraction experiments on metal alloys [1]. The main principles and equations still in use are exposed by Guinier and Fournet [2] in the very first monograph on SAXS. The development of SANS experiments started 30 years later, in the 1960s. The increase of interest was related to the pioneering work of Sturhmann et al. [3–5] where contrast variation experiments demonstrated that neutrons were a powerful tool to investigate materials. Indeed, the difference of scattering length densities between isotopes and more precisely between hydrogen and deuterium atoms is at the basis of most of the experiments. Moreover, neutrons are nondestructive and do not alter the samples as X-rays from synchrotron sources can do.

The aim of the chapter is to give an overview of what small-angle neutron scattering is. In the first three sections, the experimental aspects will be explained with the description of a SANS instrument, the course of an experiment, and the data reduction. The two following parts will be dedicated to data interpretation and analysis. Basic rules of scattering will be recalled, useful equations of form factors will be given, and the instrumental resolution combined with polydispersity (variation in particle size) effects will be presented. This chapter will conclude with the recent advancements and future developments in SANS.

## 2 Description of SANS Instruments

The two main sources of neutrons are steady-state reactors and spallation sources. In the first case, neutrons are continuously produced by fission processes. In the second case, a pulsed neutron beam (typically with 25 or 50 Hz frequency) is generated by the collision of high-energy protons which chop off heavy atoms. The time-of-flight method is used on the instruments to analyze the neutrons arriving on the detector. Consequently, the geometry and handling of SANS experiments depends on the kind of source. A world directory of SANS instruments is available on the web sites given in [6]. Technical descriptions of some of these instruments can be found in [7] as well.

The spectrometers D22 (ILL, France) and LOQ (ISIS, UK) will be described as example for steady-state and time-of-flight instrument respectively. Then, D22 characteristics will be used to illustrate different sections of the article.

## 2.1 The Steady-State Instrument D22

A typical example of steady-state pinhole instrument is D22 at the Institut Laue Langevin, Grenoble. D22 was commissioned in 1995 and has been improved with the installation of a new detector in March 2004. The schematic layout of the instrument is given in [Figure 13-1](#).

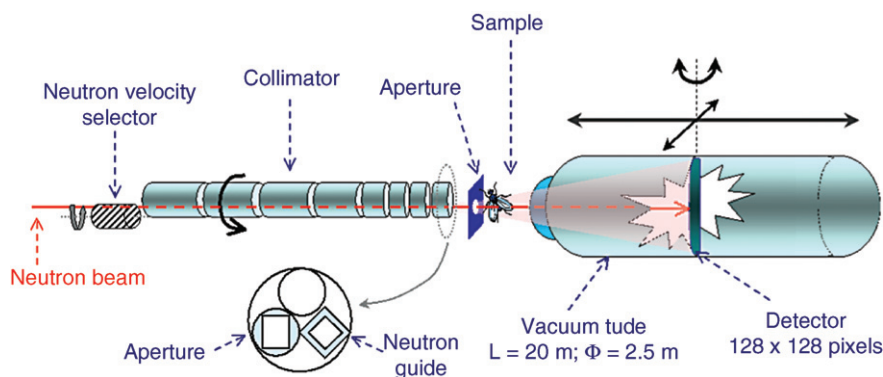


**Figure 13-1**

Schematic representation the steady-state instrument D22 at the Institut Laue Langevin (figure courtesy of the ILL)

A white beam is produced by the horizontal cold source in the reactor. The wavelength is selected through a mechanical velocity selector (DORNIER), which consists of a rotating drum with helically curved absorbing slits at its surface. The wavelength can be varied between 4.6 and 40 Å when the rotation speed decreases from 28,000 to 4,000 rpm. The wavelength spread  $\Delta\lambda/\lambda$  is 10% (FWHM). The selector is mounted on ball-bearings and forbidden frequencies of rotation exist to minimize vibrations and resonance. Silver behenate, a polycrystalline powder giving narrow Bragg peaks is used as a standard to calibrate the wavelength. Several orders of Bragg peaks are obtained within few minutes, with a first order at  $q_0 = 0.1763 \text{ Å}^{-1}$ .

The empirical relationship between the wavelength and the velocity or the RPM (revolutions per minute) follows:

$$\lambda = \frac{A}{RPM} + B \quad (1)$$

At the date of this review  $A = 121651 \text{ \AA}^{-1}$  and  $B = 0.1355 \text{ \AA}^{-1}$  on D22.

After the selector, a set of vertical and horizontal slits are mounted. They define the size of the beam. The closure of the slits to reduce the beam size is used when a higher instrument resolution is necessary, for example, to study the shape of the Bragg peaks in flux line lattices. Then neutrons pass through a low efficiency detector, called a monitor. The integrated counts during the time the measurement are used for data normalization.

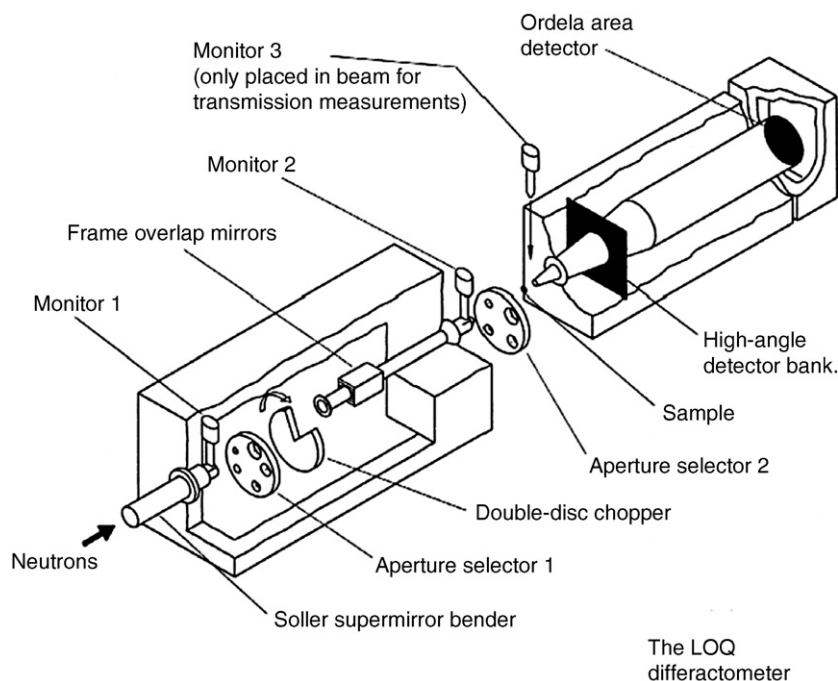
*Collimation* is a series of waveguides necessary because unlike electromagnetic radiation (light or X-Ray), neutrons cannot be easily focused. The possibility of neutron lenses will be discussed in the last section dedicated to the new perspectives for SANS instruments. The collimation part on D22 is composed by eight guides with a cross-section of  $55 \times 40 \text{ mm}^2$ . Their lengths vary as a geometrical series to yield free flight paths of 1.4–17.6 m and are calculated in such a way that when one removes or adds a part of collimation the flux decreases or increases by a factor of 2. Antiparasitic diaphragms are placed between two guide sections. At the end of the collimation, the size of the beam in front of the sample is fixed by an aperture, made of B4C covered by Cadmium. Their shapes (round, slits, square) and sizes (from 1 to 20 mm) are very flexible depending on the sample geometry. The detector moves from 1.1 to 18 m from the sample position in a 2-m diameter tube under vacuum (0.2 mbar).

The “beam-stop” made of an absorbing piece of B4C and Cadmium placed in front of the detector prevents the direct beam from damaging the detector. The possibility to offset the detector laterally up to 400 mm in the vacuum vessel allows one to cover a dynamic  $q$ -range ( $q_{\max}/q_{\min}$ ) of 20 with only one configuration. The detector rotation around its middle axis is also possible and useful at small detector distances ( $D < 2 \text{ m}$ ) to correct from geometric distortions (see [Figure 13-5](#)). By combining the entire range of wavelengths and detector distances, the total accessible  $q$ -range varies from  $8 \cdot 10^{-4}$  to  $0.8 \text{ \AA}^{-1}$ .

D22 is located close to the brilliant horizontal cold source of the reactor. Thanks to the large cross-section of the neutron guide, the short rotor and high transmission of its velocity selector, the diffractometer D22 is up to now the one with the highest flux at the sample position with up to  $10^8 \text{ neutron/s/cm}^2$ .

## 2.2 The Time-of-Flight Instrument LOQ

The schematic geometry of the LOQ instrument is shown in [Figure 13-2](#). A description of the instrument is given in [8]. The white beam passes through



■ **Figure 13-2**

**Schematic representation of the time-of-flight instrument LOQ at the ISIS Facility, Didcot, UK (figure courtesy of ISIS)**

super-mirror Soller bender which removes wavelengths less than  $2 \text{ \AA}$ , a first aperture, a disk chopper with variable openings, and a frame overlap mirrors to cut the wavelengths higher than  $12 \text{ \AA}$ . The neutrons flight through a 3-m evacuated guide. A second aperture is placed at the end of the final collimation and defines the sample beam size. The sample position is at around 11.1 m from the moderator. The sample transmissions are measured by inserting a monitor just after the sample after reducing the beam diameter to 1 mm between the sample and the monitor.

The main gas-filled multi-detector is fixed at 4.1 m from the sample in a vacuum tube. The active area is  $64 \text{ cm}^2$  with  $128 \times 128$  pixels (5 mm resolution) and 100 time channels for the different wavelengths. The high  $q$  can be measured simultaneously using a second detector set at a fixed and close position to the sample.

The principal benefit of conducting SANS experiments at ISIS is that a “white” incident beam is combined with time-of-flight detection techniques to give a very large dynamic range in scattering vector, accessible in a single measurement without any need to reconfigure the instrument.

On LOQ at ISIS a pulse shaping 25 Hz disc shopper selects wavelength of 2.2–10 Å, which are used simultaneously by time-of-flight.

For fixed geometry instruments working in time-of-flight mode, different wavelength neutrons scattered at a same angle have different  $q$  values and arrive on the detector at different times. The broader the incoming wavelength range, the wider the  $q$ -range of the instrument. The data are saved in a 3D array with two dimensions for the pixels of the detector and the third for the time axis.

The range of scattering vectors for time-of-flight instrument is similar to the range of steady-state instruments. The main advantage of time-of-flight instrument is that the full  $q$ -range is covered by only one instrument setting.

## 2.3 Detectors for SANS Instruments

Up to now, the most used detectors in SANS are gas proportional counters. Until the end of 2003, D22 was handled with the largest area multidetector filled with  $^3\text{He}$  as detection medium and  $\text{CF}_4$  as stopping gas. Technical data on neutron detection are detailed in [9]. The neutron absorption by a target isotope molecule ( $^3\text{He}$ ) induces a fission reaction and emission of two charged particles, one triton and one proton, in opposite direction with a total kinetic energy of 760 keV which induces the primary ionization in gas. The stopping gas has two roles. First it reduces the path length of the electrons for a good position resolution and minimizes the wall effects. Secondly, in an environment of high photon background, it has a low sensitivity to gamma and X-rays. The electrons are accelerated to get more ionization and to amplify the signal. Near the anode wire, where the electric field is very high, the ions produced by the electron avalanche move away from the anode and induce a current in the cathode which is measured.

On D22, the previous detector was composed by a network of  $128 \times 128$  wires with a pixel size of  $0.75 \times 0.75 \text{ mm}^2$ . The advantages of gas-filled detectors are their high efficiency for thermal neutrons, around 80% at a wavelength of 6 Å and a low sensitivity to  $\gamma$  radiation.

The maximal count rate is limited by the time to collect the charges and the electrons. The last developments on this field have permitted to decrease the dead time down to  $\tau = 1 \text{ ns}$  which represents a lost of 10% at 100 kHz count rate (neutron/s). Dead time correction is possible and strongly improves the data quality and curve overlapping. The two possible models are called paralyzable and nonparalyzable. The “real” count rate  $C_{\text{real}}$  is calculated from the measured count rate  $C_{\text{mes}}$  through the following relations.

Nonparalyzable model:

$$C_{\text{real}} = \frac{C_{\text{mes}}}{1 - \tau C_{\text{mes}}} \quad (2)$$

Paralyzable model:

$$C_{\text{real}} = C_{\text{mes}} \exp(-\tau C_{\text{mes}}) \quad (3)$$

The nonparalyzable model was used on D22 with the multiwire detector and is still in use for data correction on D11 (ILL). More details can be found in [10]. Example of determination of detector dead time is presented in [Figure 13-3](#).

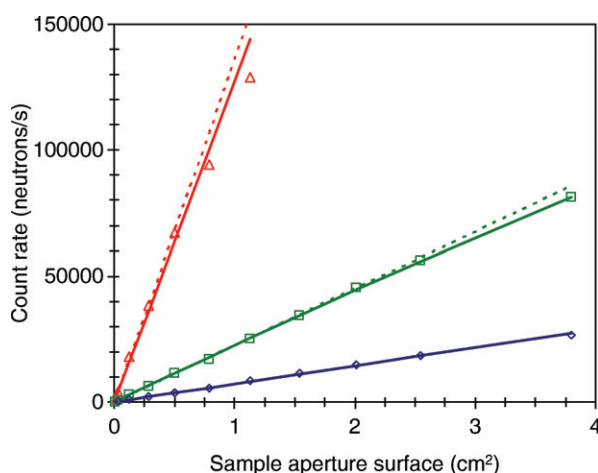


**Figure 13-3**

Dead time measurement on the gas-filled multiwire detector from D22. Flux measurement with factor of attenuation of: (◇)  $F = 147$ , (□)  $F = 902$ , (Δ)  $F = 2874$ . The dotted lines are linear functions and full lines the fitting with the nonparalyzable equation (2)

The measurement done on the multiwires gas-filled detector from D22, consists in measuring the attenuated direct beam through circular diaphragms and increasing progressively the surface of the beam at the sample position. The three attenuation factors are 147, 903, and 2,874. By considering a homogenous beam, the flux is proportional to the beam surface. The full lines are the data fitting with the nonparalyzable model, and the dotted lines are linear functions. The dead time  $\tau$  is found at 0.91 ms, which corresponds to a lost 10% for a measured count rate of 100 kHz (2).

Since March 2004, a new detector is operating on D22. The new detector developed at the ILL by the detector group is a real-time neutron detector for small-angle scattering applications, which is capable of counting 2 MHz of neutrons on the whole detector with dead time losses of not more than 10%, rather than the 100 kHz for the previous detector. This detector is composed of



an array of 128 vertical tubes of 8 mm external diameter and 102 mm length aligned side by side in a plan and brazed on both ends to a common pressure vessel. The sensitive area is  $1 \text{ m}^2$ , with a pixel size of  $0.8 \times 0.8 \text{ mm}^2$ . The tubes are filled with  $^3\text{He}$  and  $\text{CF}_4$  at 15 bars. The thin resistive anode wire is tightened in the middle of the tube and relied on both sides of the amplifiers. The conversion of neutrons to electrons follows the processes described previously. The impact position along the tubes is now measured by charge division on the anode wire. Finally, each tube is an independent counter able to reach 80 kHz at 10% dead time correction. For very high count rates or localized spots due to pragg peaks for example, a dead-time correction per tube can be performed. More details are described in [11, 12].

For description of other neutron detectors, please refer to [9, 10, 13].


## 2.4 Sample Environments

The sample environment is easily versatile to match the various needs of the users. Most of the SANS instruments possess a remotely controlled thermostatted sample changer. Cryostats, cryofurnaces, furnaces, electromagnets are also available. A vacuum chamber can be used for very low scattering samples to reduce the scattering from air.

The development of SANS experiments is strongly related to the development of new sample environments, to investigate properties of sample under nonsteady conditions. Shear apparatus, pressure cell, or stopped-flow apparatus are more and more used routinely. Special equipments may also be developed and designed by the scientist visitors (flash light [14], extruder [15], polarizer [16]) and adapted to the sample position.

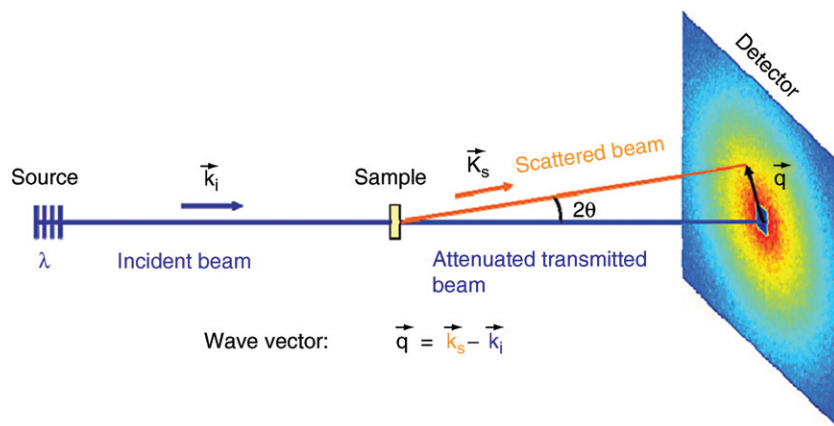
## 3 Course of a SANS Experiment

### 3.1 Definition of the q-Vector

The schematic representation of a small-angle scattering experiment is presented in  Figure 13-4. In an ideal case, the neutron beam can be viewed as an assembly of particles flying in parallel directions at a same speed. It can be described by a planar monochromatic wave which the propagation equation can be written as:

$$\phi(x, t) = \phi_0 e^{-i(kt - \omega T)} \quad (4)$$

$\omega = 2\pi/T$  is the pulsation and  $\mathbf{k}_i$  is the incident wave vector; the magnitude is  $k = 2\pi/\lambda$ . An atom scattered in the beam gives raise to a spherical wave. In SANS, only the coherent elastic interaction between the neutron beam and the sample is



■ Figure 13-4

Schematic representation of a scattering experiment and representation of the scattering vector  $\mathbf{q}$  in the detector plan

considered. The only thing which changes is the direction of the wave vector  $\mathbf{k}_s$ . The scattering vector (or wave vector or momentum transfer)  $\mathbf{q}$  is the difference between incident and scattered wave vectors ( $\mathbf{q} = \mathbf{k}_s - \mathbf{k}_i$ ). By definition, the angle between  $\mathbf{k}_s$  and  $\mathbf{k}_i$  is called  $2\theta$ . The magnitude of  $\mathbf{q}$  quantifies the lengths in the reciprocal space and is expressed in  $\text{\AA}^{-1}$  or  $\text{nm}^{-1}$

$$q = \frac{4\pi}{\lambda} \sin \theta. \quad (5)$$

If one introduces the latter equation in the Bragg law, one obtains:

$$q = \frac{2\pi}{d}. \quad (6)$$

This simple relation links the lengths in direct and reciprocal spaces and allows one to define the observation window during the experiment.

The aim of the following section is to describe the experiment course step by step starting from the choice of the configuration up to the data acquisition.

## 3.2 Choice of Configurations and Systematic Required Measurements

Before starting an experiment, it is necessary to think about the  $q$ -range required and to optimize the configurations needed. By configuration one means the wavelength, the sample-to-detector distance  $D$ , the collimation  $C$  and the detector offset (if possible on the instrument). In most of the cases the total  $q$ -range offered

by the instrument is not necessary, and the limited beam time allocated per experiment does not allow the users to investigate all the instrument possibilities.

If the largest size  $L$  of scatterers is roughly known (from any other technique), an evaluation of the minimum  $q$  is obtained by  $\pi/L$ . With a steady-state instrument, it is recommended if possible to keep the wavelength constant and to vary the sample-to-detector distance to cover the needed  $q$ -range. This choice avoids repeating the transmission measurements and the calibrations that are wavelength-dependent. It also facilitates the data treatment.

### 3.2.1 Collimation

The choice of the collimation distance is a compromise between the size of the direct beam (and thus the resolution, see [Section 6](#)) and the flux. Usually, a collimation distance matching the sample-to-detector distance is used. Nevertheless, for strong scatterer like water and/or short sample-to-detector distance, larger collimation distances can be used to reduce the flux and the scattering and to avoid detector saturation and damage.

A frequently chosen set of configurations on D22 is:  $\lambda = 6 \text{ \AA}$ ,  $D = 17.5, 5$ , and  $1.4$  with an offset of the detector of  $400 \text{ mm}$  to cover a  $q$ -range from  $2 \cdot 10^{-3}$  to  $0.65 \text{ \AA}^{-1}$ .

The beginning of an experiment for each configuration requires, the alignment of the beam-stop and measurement of beam center, electronic background, scattering of the sample empty cell and of a standard sample for absolute calibration.

### 3.2.2 Beam Center Determination

An attenuator is set in the direct beam and the beam-stop is removed. The attenuated direct beam is measured through an empty position during several tens of seconds. The beam center of gravity is calculated with standard routines and further used for radial averaging. The integrated number of neutrons in the direct beam allows one to calculate the flux if the attenuation factor is known.

### 3.2.3 Beam-Stop Alignment

The position of the direct beam on the detector varies with the sample-to-detector distance, the collimation, and in an important way with the wavelength since neutrons fall under gravity. Thus, the beam-stop position varies and the

alignment has to be checked for each configuration, especially for large wavelengths and large sample-to-detector distances. A strong forward scatterer (teflon, graphite, etc.) allows one to clearly see the shadow of the beam-stop, which is correctly aligned when the same number of neutrons is counted on the beam-stop edges (or on the first significant channel).

### 3.2.4 Electronic Background

The background is measured by stopping the incoming beam with a piece B4C or Cadmium, which are both strong neutron absorbers (but Cd creates gammas). In consequence what is measured on the detector comes from electronic noise, cosmic, and instrument environment. These backgrounds are generally low. Measurements are really important for weak scattering samples.

### 3.2.5 Standard for Calibration

The use of a standard has two functions: correction of the variation in cell efficiency and normalization in absolute unit. Another possibility to get the absolute scaling is to use standards with known cross section [17, 18]. For SANS, samples with predominant incoherent scattering such as water (H<sub>2</sub>O) or vanadium are currently used for the absolute scaling. With an ideal detector, water shows a flat scattering independent from the scattering angle.

The water scattering is not measured at large sample-to-detector distances and long collimation because the low flux would require several hours of acquisition to get a good signal to noise ratio. The normalization and correction of cell efficiency are done with a water run measured in another configuration but with the same wavelength. The correction of flux and solid angle is explained in the next section.

It is recommended to perform the instrument calibrations and standard measurements at the beginning of the experiment. Indeed, in case of instrument failure, it will be nevertheless possible to treat the data recorded.

### 3.2.6 Transmission

The sample transmission is the ratio between the flux through the sample and the incident flux at  $q = 0$ . The attenuated flux by the sample is measured in the same way and conditions as the direct beam. A transmission measurement lasts less than 5 min.

### 3.2.7 Counting Time

For many samples, the scattering at large angles is strong but mainly due to incoherent scattering coming from the sample and the solvent, especially for hydrogenated solvent. Depending on the instrument and on the detector it is known that a certain total number of neutrons  $N_T$  on the whole detector area will give after the radial averaging (in case of isotropic scattering) a good statistics, i.e., small error bars and smooth shape of the curve. For example, on D22,  $N_T = 4,000,000$  counts give good statistics. Short acquisitions of 10 s or less allow one to estimate the sample count rate  $c/s$ .  $N_T$  divided by  $c/s$  gives an estimation of the acquisition time. The development of new “intelligent program” able to stop an acquisition when a certain number of neutrons is reached on the whole detector or in a defined area will be discussed in the last section “future and development.”

The relevant count rate is the difference of count rates between the sample and the solvent (mainly coming from incoherent diffusion). A too short measurement especially at high  $q$  where the coherent intensity decreases give large error bars on the absolute intensity and even negative values after subtraction of background and incoherent scattering. It is recommended to measure the solvent at large angles to have an experimental determination of the level of incoherent scattering.

The number  $N_T$  is of course just an indication that must be modulated in function of the kind of information needed and also in function of the allocated beam time. It can be reduced if statistics is not really needed (for example, measurement of a slope) or increased in contrary if statistics is required (determination of a minimum, shape of Bragg peaks, etc.).

### 3.2.8 Command Files

Once the previous steps have been done, the configuration settings and the acquisitions can be programmed in command files.

## 3.3 Conclusion

The choice of the configurations may be a determining factor for further analysis and data fitting. It is a compromise between flux, resolution, beam time allocated, and number of samples.

## 4 From Raw Data to Absolute Scaling

The instruments from different Institutes have developed data treatment programs, which can be adapted to other instruments after minor modifications for the reading of data and parameters. The principle remains similar. For the ILL SANS instruments see [19] for the standard programs in use. The different steps consist in:

- Calculating the beam center for the different configurations used.
- Creating mask files to hide cells behind the beam stop as well as potential “bad cells”
- Calculating transmissions.
- Performing radial averaging giving the intensity as a function of  $q$  in case of isotropic scattering. Depending on the programs, what is called “intensity” at this step can be a number of neutrons, or a count rate per second or per monitor unit.
- The last step to obtain the absolute intensity is more delicate and its description is the aim of the following section.

(1) Note: The two last points can be performed in the reverse order. Absolute scaling can be performed on the 2D image, before radial or section averaging for anisotropic data.

When a coherent beam with a flux  $\Phi_0$  illuminates a sample of volume  $V$  and a thickness  $e$ , during a time  $t$ , a given fraction of the incident flux  $\Delta N$  is elastically scattered in the direction  $q$  within a solid angle  $\Delta\Omega$ :

$$\Delta N = \Phi_0 t Tr \frac{d\sigma}{d\Omega}(q) \Delta\Omega, \quad (7)$$

where  $Tr$  is the transmission of the sample.

$\frac{d\sigma}{d\Omega}(q)$  is the differential scattering cross section characteristic of elastic interaction between sample and neutrons. Then the intensity  $I$  scattered per unit volume is

$$I(cm^{-1}) = \frac{1}{V} \frac{d\sigma}{d\Omega}(q) = \frac{\Delta N(q)}{\Phi_0 Tr(\Delta\Omega).t.e}$$

$$\left(\frac{d\Sigma}{d\Omega}\right)_{\text{Total}} = \frac{N(q)}{\Phi_0 \cdot \Delta\Omega(q) \cdot Tr \cdot t \cdot e} = \frac{1}{\Phi_0 \Delta\Omega(q) \cdot Tr(q) \cdot t \cdot e(q)} I(q). \quad (8)$$

In soft condensed matter, the samples are generally filled in a quartz cell that contributes slightly to the general scattering. The scattering from the empty cell (EC) is subtracted from the total scattering as follows:

$$\left(\frac{d\Sigma}{d\Omega}\right)_{\text{sample}} = \frac{1}{e_{\text{sample}}} \left[ \frac{N_{\text{sample}}(q)}{\Phi_0 \cdot \Delta\Omega(q) \cdot Tr_{\text{sample}} \cdot t_{\text{sample}}} - \frac{N_{\text{EC}}(q)}{\Phi_0 \cdot \Delta\Omega(q) \cdot Tr_{\text{EC}} \cdot t_{\text{EC}}} \right]_{\text{sample}} \quad (9)$$

$$= \frac{1}{e_{\text{sample}} \Phi_0} \left[ \frac{N_{\text{sample}}(q)}{\Delta\Omega(q) \cdot Tr_{\text{sample}} \cdot t_{\text{sample}}} - \frac{N_{\text{EC}}(q)}{\Delta\Omega(q) \cdot Tr_{\text{EC}} \cdot t_{\text{EC}}} \right]$$

(2) In the case of a solid sample, which does not necessitate a cell, the scattering from air has to be removed.

The transmissions are calculated with respect to the empty beam.

We now turn to the description, calculation, or measurement of the different terms of the previous equation.

## 4.1 Determination of the Incident Flux $\Phi_0$

In (7), the incident flux  $\Phi_0$  is the number of neutrons per second at the sample position for a given aperture. The flux can be measured directly with a calibrated monitor installed at the sample position. The other possibility is to measure the direct beam on the detector through a calibrated attenuator. This approach calls  $\Sigma_{EB}$ , the sum of neutrons integrated in the surface of the direct beam,  $t_{EB}$ , the acquisition time, and  $F$ , the factor of attenuation. Then, taking into account the detector dead time  $\tau$

$$\Phi_0(n/s) = F \frac{\Sigma_{EB}/t_{EB}}{1 - \tau \Sigma_{EB}/t_{EB}}. \quad (10)$$

Thanks to the development of new fast detectors like the one on D22 at the ILL, the dead time correction is not necessary in most of the cases. For classical gas detectors, the dead time is of the order of few tens of microseconds and corresponds to a lost of 10% of neutrons at count rates of 100 kHz.

## 4.2 Normalization with a Standard Sample

Samples with predominant incoherent scattering such as light water ( $H_2O$ ) or vanadium are used for the absolute scaling and to correct the variations in efficiency of the cells.

$$\left(\frac{d\Sigma}{d\Omega}\right)_{\text{sample}} = \frac{I_{\text{sample}}}{I_{\text{standard}}} \left(\frac{d\Sigma}{d\Omega}\right)_{\text{standard}} \quad (11)$$

A water sample of thickness  $e = 0.1$  cm is frequently used as standard because water is easy to find, the liquid is homogenous at the scales of SANS, and the scattering is mainly incoherent. However, due to inelastic and multiple scattering effects, the water scattering is not totally isotropic, but stronger in the forward direction. The assumption that the neutrons that are not transmitted are scattered uniformly in  $4\pi$  steradians is wrong. A wavelength-dependent correction factor  $g(\lambda)$  has to be introduced to write the real scattering cross section

$$\left(\frac{d\Sigma}{d\Omega}\right)_{\text{H}_2\text{O}}^{\text{real}} = g(\lambda) \frac{1 - Tr}{4\pi.e.Tr}. \quad (12)$$

In SANS there is no universal calibration curves. The water scattering measured on two instruments may vary significantly. Because of multiple scattering and inelastic effects, scattering depends on the wavelength distribution, on the geometry and configuration, and on the detector. Between D11 and D22, when both instruments are working with a gas-filled detector, the difference of  $g(\lambda)$  values was of the order of few percents. As long as possible, it is thus extremely important to carry out the calibrations in the same setting conditions as the samples.

$(d\Sigma/d\Omega)_{\text{H}_2\text{O}}^{\text{real}}$  can be calculated using (9). It is also possible to recalculate  $(d\Sigma/d\Omega)_{\text{H}_2\text{O}}^{\text{real}}$  by measuring standards (polymer) from samples with a known cross section [17, 18].

$(d\Sigma/d\Omega)_{\text{H}_2\text{O}}^{\text{real}}$  as a function of  $\lambda$  may be empirically extrapolated with a polynomial function:

$$(d\Sigma/d\Omega)_{\text{H}_2\text{O}}^{\text{real}} = A + B.\lambda + C.\lambda^2 + D.\lambda^3$$

The water cross-section increases with the wavelength and varies slightly with temperature. The values are close to  $1 \text{ cm}^{-1}$ .

Sample normalization using water as standard is obtained according the following equation:

$$\left(\frac{d\Sigma}{d\Omega}\right)_{\text{sample}} = \frac{1}{F_{\text{sc}}} \left(\frac{d\Sigma}{d\Omega}\right)_{\text{H}_2\text{O}}^{\text{real}} \frac{\left[\frac{I_{\text{sample}} - I_{\text{B4C}}}{Tr_{\text{sample}}} - \frac{I_{\text{sample-EC}} - I_{\text{B4C}}}{Tr_{\text{sample-EC}}}\right] \frac{1}{e_{\text{sample}}}}{\left[\frac{I_{\text{H}_2\text{O}} - I_{\text{B4C}}}{Tr_{\text{H}_2\text{O}}} - \frac{I_{\text{H}_2\text{O-EC}} - I_{\text{B4C}}}{Tr_{\text{H}_2\text{O-EC}}}\right] \frac{1}{e_{\text{H}_2\text{O}}}} \quad (13)$$

The subscript EC refers to the empty cell.  $Tr$  is the transmission with respect to the empty beam,  $I$  is the number of neutrons per second.  $F_{\text{sc}}$  is a scaling coefficient equal to 1 when the water and the sample are measured in the same instrument configuration. For large sample-to-detector distance ( $D > 10 \text{ m}$ ) and thus large collimation, the flux and water count rates are too low to get a good statistics in a reasonable time. A water run measured in a configuration with higher flux (at shorter sample to detector distance) but the same  $\lambda$  is used to correct the variations of detector efficiency. Then, the scaling factor  $F_{\text{sc}}$  corrects the flux that varies with the collimation and the solid angle according to

$$F = \frac{(\Phi_0 \Delta\Omega)_{\text{sample}}}{(\Phi_0 \Delta\Omega)_{\text{H}_2\text{O}}} = \left(\frac{\text{Coll}_{\text{H}_2\text{O}} D_{\text{H}_2\text{O}}}{\text{Coll}_{\text{sample}} D_{\text{sample}}}\right)^2 = \frac{\Phi_{\text{sample}}}{\Phi_{\text{H}_2\text{O}}} \left(\frac{D_{\text{H}_2\text{O}}}{D_{\text{sample}}}\right)^2, \quad (14)$$

where  $D_{\text{sample}}$  and  $D_{\text{water}}$  are the sample-to-detector distances;  $\text{Coll}_{\text{sample}}$  and  $\text{Coll}_{\text{water}}$  are the collimations, and  $\Phi_{\text{sample}}$  and  $\Phi_{\text{water}}$  are the fluxes at the sample position in the two configurations.



The other possibility to calculate  $(d\Sigma/d\Omega)_{\text{H}_2\text{O}}^{\text{real}}$  is to apply (2), the delicate point being the accurate measurement of  $\Phi_o$ .

### 4.3 Solid Angle $\Delta\Omega(Q)$

► Figure 13-5 presents the geometry of a scattering experiment when the detector is close to the sample position. The scales are not respected in order to put in evidence the different angles and distances. O is the origin of the scattered beams (sample position) and O' the image of the direct beam on the detector.  $2\theta$  is the scattering angle  $O'O''$ , also equal to the angle defined by  $ADA'$ . The sample-to-detector distance is represented by the segment  $D(2\theta) = \overline{OO'}$  and  $p = \overline{A'B'}$  is the pixel size.  $D(0) = \overline{OO'}$

The sample-to-detector distance and the solid angle are function of  $2\theta$  according to

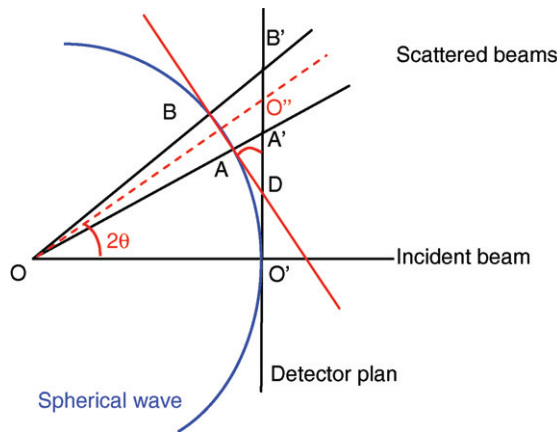
$$\Delta\Omega(2\theta) = \overline{AB}^2 / [D(2\theta)]^2,$$

$$D(2\theta) = D(2\theta = 0) / \cos(2\theta) \text{ and } \overline{AB} = p^2 \cos(2\theta).$$

Finally

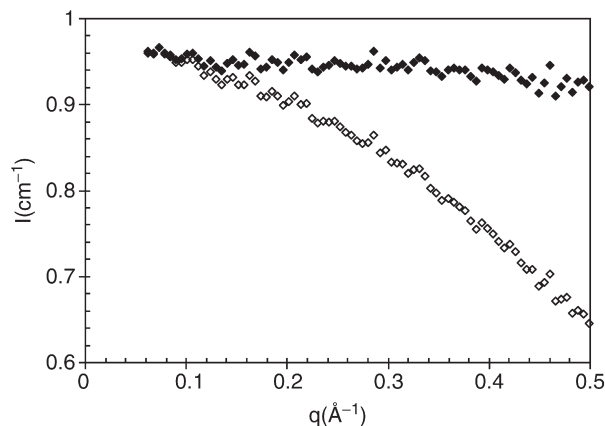
$$\Delta\Omega(2\theta) = \frac{p^2 \cos^3(2\theta)}{D(2\theta = 0)}. \quad (15)$$

Equation (15) shows that the solid angle value decreases with  $q$ . An example is shown in ► Figure 13-6, where water was measured with the following configuration:  $D = 1.4$  m,  $C = 17.6$  m, and  $\lambda = 6$  Å. The data are normalized in absolute



■ Figure 13-5

Geometric representation of scattered beams: determination of detector distance and solid angle as a function of  $2\theta$ , the scattering angle



■ Figure 13-6

Water scattering measured on D22 at short sample-to-detector distance,  $D = 1.4$  m,  $C = 17.6$  m,  $\lambda = 6$  Å. The raw data are normalized in absolute scale according to (1.8). ( $\diamond$ )  $\Delta\Omega$  kept constant at  $p^2/D(0)^2$ ; ( $\blacklozenge$ )  $\Delta\Omega$  calculated with (15) to correct from geometric distortion

scale according to (8). The hollow diamonds are obtained taking the solid angle as a constant. One observes a strong decrease of the intensity as  $q$  increases. The full symbols are calculated using (15) which allows one to get the flat scattering expected for incoherent scatterers. The slight decrease still remaining at high  $q$  can be due to inelastic effects in light water.

## 4.4 Transmission

### 4.4.1 Definition

The transmission is the ratio of the intensities at  $q = 0$  between the beam through the sample and the white beam. It depends on the sum of coherent, incoherent, and absorption cross-sections and also from the scattering angle.

$$\text{Tr}(2\theta, \lambda) = \frac{I(2\theta)}{I_0} = \exp(-\mu(\lambda)e(2\theta)),$$

$$\text{Tr}(\lambda) = \frac{I(0)}{I_0} = \exp(-N\sigma(\lambda)e(2\theta)) = \exp(-\mu(\lambda)e(2\theta)) = \exp(-e(2\theta)/\Lambda(\lambda)), \quad (16)$$

Where  $\mu(\lambda)$ , the mass adsorption coefficient is wavelength-dependant and  $\Lambda(\lambda)$  is the mean free path of the radiation in the sample.  $\sigma(\lambda)$  can be calculated from the transmission measured at  $\theta = 0$  and is the sum of three terms:

$$\sigma(\lambda) = \sum_i \sigma_{\text{coh},i} + \sigma_{\text{incoh},i} + \sigma_{\text{abs},i}(\lambda) \quad (17)$$

Table 13-1

Length scattering densities, coherent, incoherent and absorption cross-sections for selected atoms and their isotopes [20]

Nucleus or isotope	B ( $10^{-15}$ m)	$\sigma_{\text{coh}}$ ( $10^{-24}$ cm <sup>2</sup> )	$\sigma_{\text{incoh}}$ ( $10^{-24}$ cm <sup>2</sup> )	$\sigma_{\text{abs}}$ ( $10^{-24}$ cm <sup>2</sup> )
<sup>1</sup> H	−3.739	1.7568	80.26	0.3326
<sup>2</sup> D	+6.671	5.592	2.05	$5.19 \times 10^{-4}$
<sup>3</sup> He	+5.74–1.483i	4.42	1.6	5333
<sup>4</sup> He	+3.26	1.34	0	0
<sup>10</sup> B	−0.161–1.66i	0.144	3	3835
<sup>11</sup> B	+6.65	5.56	0.21	0.0035
C	+6.646	11.01	0.5	1.9
N	+9.36	1.34	0	0
O	+5.803	4.232	0	0.0001
Na	+3.63	3.59	1.62	0.53
Si	+4.107	2.12	0	0.177
Cl	+11.65	17.06	4.7	44.1
V	−0.3824	0.0184	5.08	5.08
Cd	+4.87–0.70i	3.04	6.5	2520
Pb	+5.91	4.39	0.093	6.9
Gd	+6.56–13.82i	29.3	151	49700

$\sigma_{\text{abs}}(\lambda)$  the absorption cross-section is due to nuclear capture process. It is inversely proportional to the amplitude of the wave vector  $k = 2\pi/\lambda$  and thus proportional to  $\lambda$ . The values for a neutron velocity of 2200 m/s ( $1.8 \text{ \AA}$ ) are given in Table 13-1. Then, for a wavelength  $\lambda$ ,  $\sigma_{\text{abs}}(\lambda) = \sigma_{\text{abs}}(\lambda)/1.8$ .

The absorption cross sections of selected nuclei and isotopes are listed in Table 13-1. Typical values range from 0.1 to 10 barns ( $10^{-24} \text{ cm}^2$ ) but can be very high for certain atoms like Boron and its isotope B(768 and 3,835 barns), Cadmium (2,520 barns), or Gadolinium (49,700 barns). Consequently, these very absorbent materials are widely used as shielding (beam-stop, coverage inside walls of the detector tube, etc.).

$\sigma_{\text{coh}}$  and  $\sigma_{\text{incoh}}$  are the apparent absorptions due to coherent and incoherent scattering.

## 4.4.2 Numerical Applications and Examples

In the soft condensed matter field, where hydrogen atoms are largely present, the amount of hydrogen or deuterium has a large impact on the transmission. The measured transmissions of 1 mm of H<sub>2</sub>O and D<sub>2</sub>O at  $6 \text{ \AA}$  are 0.52 and 0.93, respectively.

The absorption of air is of 1% per meter. For long instruments as SANS spectrometers, it is then important to keep the neutron guides and the detector tank under vacuum. In some cases,  $^4\text{He}$  is used to fill the neutron guides. A guide of 1 m length filled with  $^4\text{He}$  at atmospheric pressure is considered. Helium density is  $d = 0.2 \text{ g/cm}^3$ . The molecule number per  $\text{cm}^3$  is  $d_N = dN_a/M$ , with  $N_a$  the Avogadro number and  $M$  the molar mass. For a length of 1 m, the transmission is  $\text{Tr} = \exp(-d_N \sigma_T L)$ , with  $d_N = 0.301 \times 10^{20} \text{ mol/cm}^3$ ,  $\sigma_T = 1.34 \times 10^{-24} \text{ cm}^2$ , and  $L = 100 \text{ cm}$ , then  $\text{Tr} = 0.996$ . The absorption is nearly negligible, much weaker than air. Now with  $^3\text{He}$  in the same conditions,  $\sigma_T \approx \sigma_a = 5333 \times 10^{-24} \text{ cm}^2$  and  $\text{Tr} \approx 10^{-7}$ .

#### 4.4.3 Transmission at Large Angles

Does the transmission depend on the scattering angle? As for the solid angle calculation, the question can be raised for scattering measured at small detector distances and thus high scattering angles. The path length of the beam is different from the sample thickness  $e$  at large angles (Figure 13-7). A beam scattered at a position  $x$  from the entrance window traverses a length  $l$  calculated in (18).

$$l(2\theta) = x + (e - x)/(\cos(2\theta)) \quad (18)$$

We introduce the function:  $f(2\theta) = -1 + 1/\cos(2\theta)$ . Equation (18) becomes:

$$l(2\theta) = e + x[f(2\theta)] \quad (19)$$

Before interaction the beam is attenuated by a factor  $\exp(-\mu x)$  and after interaction by a coefficient  $\exp(-\mu(e - x)/\cos(2\theta))$ . Hence, the transmission is:

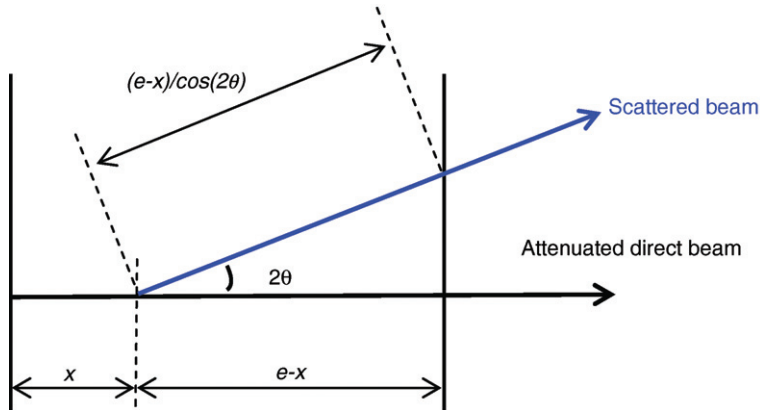


Figure 13-7  
 Path length of a scattered beam

$$Tr(2\theta) = \frac{1}{e} \int_0^e \exp[-\mu(e + xf(2\theta))] dx = \frac{1}{e} \exp(-\mu e) \int_0^e \exp[-\mu xf(2\theta)] dx \quad (20)$$

$$Tr(2\theta) = [\mu ef(2\theta)]^{-1} \exp(-\mu e) \{1 - \exp[-\mu ef(2\theta)]\}$$

The dependence of transmission as a function of  $2\theta$  and  $q$ , is presented for light and heavy water in Figure 13-8. At  $q = 0.8 \text{ \AA}^{-1}$  the diminution of the transmission is of only 3% for  $D_2O$  and can be neglected. The decrease is of 23% for  $H_2O$  and a connection must be taken into account during data reduction.

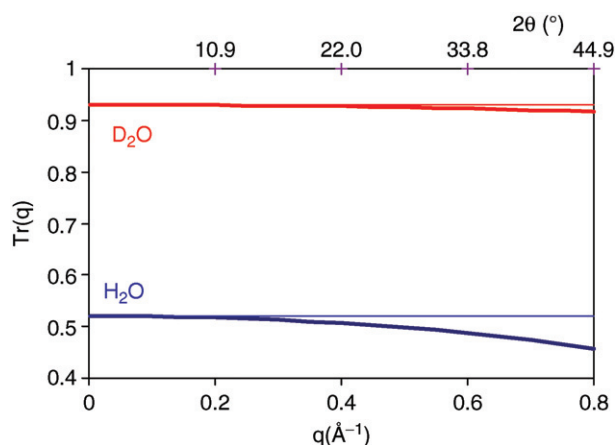


Figure 13-8

Transmission of light and heavy water as a function of the scattering angle and scattering vector. For  $\lambda = 6 \text{ \AA}$ ,  $\mu(H_2O) = -6.539 \text{ cm}^{-1}$  and  $\mu(D_2O) = -0.726 \text{ cm}^{-1}$  calculated from experimental transmission measurements on D22

## 4.5 Multiple Scattering

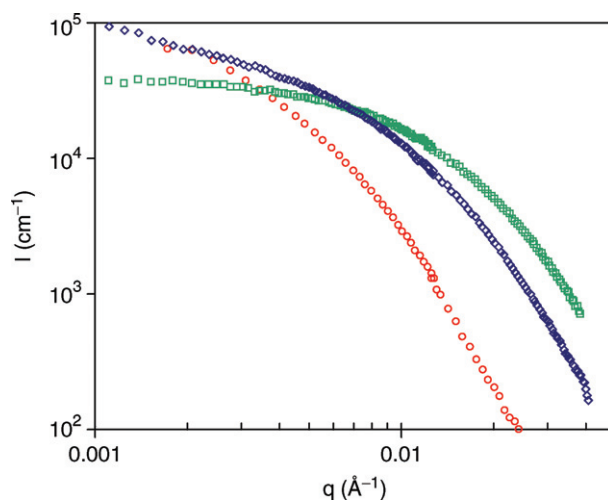
Multiple scattering occurs when a scattered neutron is scattered again in the sample. There is always a probability that such event occurs but it must not dominate the total scattering. Multiple scattering smears the true intensity since the total intensity is the sum of intensities due to single, twice, or more scattering vectors at unknown angles. The data interpretation becomes nearly impossible or wrong, if the multiple scattering is not detected. Suspicion of multiple scattering can be done in case of low transmission ( $<0.5$ ) and strong scattering intensity at low  $q$  ( $>10^4 \text{ cm}^{-1}$ ). There is no general method to correct data from multiple scattering but in case of “weak” multiple scattering, different methods are proposed [21]. A criterion to

avoid multiple scattering has been given in [22] and says that “part of attenuation of the direct beam due to coherent scattering should not be  $<9$ .” This result has been established with studies on interpenetrating polymer networks.

### 4.5.1 Transmission at Large Angles

In case of low multiple scattering, the effect is not easily detected. Different scattering distortions are observed. First evidence is that several curves measured at different configurations do not overlap. In case of fractal dimension, at low  $q$ , the multiple scattering induces a lowering of the intensity that could be confused with a plateau. Artifacts due to multiple scattering are presented in [Figure 13-9](#). The sample consists in a dispersion of carbon black particles in a matrix made of styrene-butadiene rubber [23]. The green squares ( $\square$ ) corresponds to a sample thickness  $e = 1.3$  mm, measured at  $\lambda = 20$  Å (transmission  $Tr = 0.02$ ). The data reach a plateau at  $q = 0.01$  Å<sup>-1</sup>. The blue diamond ( $\diamond$ ) have been obtained with a half-thickness sample,  $e = 0.63$  mm and  $\lambda = 20$  Å ( $Tr = 0.08$ ). The down-turn is less pronounced but still present. The last curve ( $\circ$ ) where the thickness is only 1 μm was measured at  $\lambda = 5$  Å ( $Tr = 0.88$ ). After comparison with X-ray data (not shown), it has been proved that only the latter curve does not suffer from multiple diffusion.

With concentrated microemulsions, it has been observed on the contrary, an increase in the low  $q$  scattering and of the width of the correlation peak, with a



■ Figure 13-9

Evidence of multiple scattering on a sample made of carbon black particles dispersed in an elastomer matrix. ( $\square$ )  $e = 1.3$  mm,  $\lambda = 20$  Å; ( $\diamond$ )  $e = 0.63$  mm,  $\lambda = 20$  Å; ( $\circ$ )  $e = 1$  μm,  $\lambda = 5$  Å

multiple image of the main scattering peak and an increase of the incoherent background [24].

### 4.5.2 How to Prevent Multiple Scattering?

- Use thinner sample, use diluted sample (if dilution does not induce phase transition)
- Use shorter wavelength to increase the mean free path  $\Lambda(\lambda)$
- Decrease the contrast  $\Delta\rho$  (for example, use deuterated compound in deuterated matrix)

## 4.6 Subtraction of Incoherent Background

The incoherent scattering, mainly coming from the hydrogen molecules, gives rise to a flat background that is necessary to subtract before the data analysis. The subtraction is a delicate point, since an under or upper estimation of the incoherent background may vary a slope or the position of a minimum in  $q$  and thus alter the data interpretation. Different methods are then employed.

- The incoherent background can be estimated with the measurement at the highest possible scattering vector  $q$  ( $>0.4 \text{ \AA}^{-1}$ ) because in most of the cases in soft condensed matter the objects are big and the coherent scattering becomes negligible.
- In case of very dilute deuterated compound in hydrogenated solvent, the subtraction of the scattering from the solvent will be sufficient.
- A reference sample with no structure and containing the same amount of H and D molecules (for example, a mixture of  $\text{H}_2\text{O}/\text{D}_2\text{O}$ ) can be measured. This requires to know exactly the sample composition or to prepare a mixture having the same transmission as the sample.
- If the scattering cross section as a  $q$  dependence, one can write:

$\frac{d\Sigma}{d\Omega} \propto Aq^{-d} + B$ , where  $B$  represents the background. At high  $q$ , one can suppose that the Porod regime is reached, then  $d\Sigma/d\Omega q^4 \propto A + Bq^4$ . The slope gives the value of the incoherent background. This simple empirical method gives reasonable results.

- The incoherent background can be calculated in principle with the tabulated values of  $b_{\text{inc}}$ . Nevertheless, the values are given for bound atoms, and are smaller than the real ones. Moreover, the incoherent contribution coming from the spin is not taken into account.

## 4.7 Conclusion

The data reduction is a crucial step before data analysis. Particular care must be taken in the high-angle scattering due to corrections for the solid angle, transmission and the incoherent scattering, as described in a recent article [24].

The importance of the absolute calibration is obvious. SANS curves obtained on different spectrometers or in different  $q$ -ranges can be joined together and compared. Absolute intensity allows one to calculate molecular mass, volume fraction, specific area of scattering elements, etc. It also can prove the presence of multiple scattering, repulsive or attractive forces, unexpected aggregation, or sample degradation. In addition length scattering densities can be extracted and hydration numbers deduced.

The experimental intensity in absolute scale  $\text{cm}^{-1}$  as a function of the scattering vector  $q$  is now established. The standard models to be compared with the experiment will be described in the following section.

## 5 Modeling of the Scattered Intensity

A detailed theory of small-angle scattering can be found in [2, 25]. In this section, only the basis equations will be introduced and stress will be put on analytic expressions widely used and illustrated by recent experiments.

The interaction with the neutron beam depends on the kind of atom  $i$ . The scattering probability is proportional to a surface  $\sigma_s^i$ , characteristic from the interaction between the radiation and the atom. This surface is the scattering cross section and corresponds to the atom surface seen by the radiation. The cross section is equal to  $\sigma_s^i = 4\pi \langle |b^i|^2 \rangle$ .  $b^i$  is the scattering length which characterizes the range of interaction. The scattering length density (SLD) is then equal to  $\rho(r) = \sum \rho_i(r) b^i$ , where  $\rho_i(r)$  is the local density of atom  $i$ . Basic relationships between the neutron scattering lengths and cross sections, dependencies on the spin and values are tabulated in [20]. Some of them are given in [Table 13-1](#).

The differential cross-section is related to the amplitude of the scattered wave by

$$\frac{d\sigma}{d\Omega} = |b|^2.$$

### 5.1 Rules of Thumb in Small-Angle Scattering

We consider a statically isotropic system where the particle positions are not correlated at long range. In the Born approximation, the interaction with a



scatterer does not depend on the scattering by the other scatterers. In this case, the amplitude scattered by the different particles can be added. For a particle of length scattering density  $\rho(r)$ , the amplitude is given by:

$$A(q) = \int_V \rho(r) e^{-iqr} dr \quad (21)$$

$\rho(r)$  describes the distribution of length densities in the particle and is directly related to the chemical composition. It is convenient to split  $\rho(r)$  into two parts and to put in evidence the fluctuations around an average value:

$$\rho(r) = \langle \rho \rangle + \delta\rho(r). \quad (22)$$

The contribution from the average term is null for  $q > 0$ , then

$$A(q) = \int_V \delta\rho(r) e^{-iqr} dr. \quad (23)$$

The detector measures the intensity which is the absolute square of the amplitude. The scattered intensity per unit volume is:

$$I(q) = \frac{A(q)A^*(q)}{V} = \frac{1}{V} \iint_{VV} \delta\rho(r) \delta\rho(r') e^{-iq(r-r')} dr dr'. \quad (24)$$

In the simplest case where the system is made of two phases, one of length scattering density  $\rho_p$  and the second one of length scattering density  $\rho_s$ , (24) becomes:

$$I(q) = \frac{1}{V} (\rho_p - \rho_s)^2 \iint_{V_p V_p} e^{-iq(r-r')} dr dr' = \frac{1}{V} \Delta\rho^2 \iint_{V_p V_p} e^{-iq(r-r')} dr dr' \quad (25)$$

$\Delta\rho$  is the difference of length scattering densities between particle and matrix. An assembly of  $N_p$  identical particles is next considered. Equation (25) can be rewritten as:

$$I(q) = \frac{V_p^2}{V} N_p \Delta\rho^2 [F(q)]^2, \quad \text{with } F(q) = \frac{1}{V_p} \int_{V_p} e^{-iqr} dr, \quad (26)$$

Finally, with the usual notations, one gets:

$$I(q) = \Phi V_p \Delta\rho^2 P(q) \quad (27)$$

$P(q)$  is called the particle form factor and describes the geometry of the scattering object.  $P(q)$  tends to 1 for  $q = 0$ .

We consider now an assembly of  $N_p$  identical particles correlated in space. The measured intensity is equal to the statistical average over all the particle positions and orientations in a volume  $V$ :

$$I(q) = \frac{A(q)A^*(q)}{V} = \frac{1}{V} \left\langle \int_V \rho(r) e^{-iqr} dr \int_V \rho(r') e^{-iqr'} dr' \right\rangle \quad (28)$$

Let us write  $r$  as  $r = r_i + u$ ,

$$I(q) = \frac{1}{V} \left\langle \sum_i e^{-iqr_i} \int_{V_p} \rho(u) e^{-iqu} du \sum_j e^{-iqr_j} \int_{V_p} \rho(v) e^{-iqv} dv \right\rangle \quad (29)$$

For spherical particles with identical interactions, the average of the product is equal to the product of the averages, then:

$$I(q) = \frac{N}{V} \left\langle \left[ \frac{1}{N} \sum_{i=1}^N \sum_{j=1}^N e^{-iq(r_i - r_j)} \right] \left[ \int_{V_p} \int_{V_p} \rho(u) \rho(v) e^{-iq(u-v)} du dv \right] \right\rangle. \quad (30)$$

One recognizes in the second term the particle form factor. The first term is the structure factor  $S(q)$  describing the correlation between particle mass centers. If one excludes the case  $r_i = r_j$  then the expression for the structure factor becomes:

$$S(q) = 1 + \frac{1}{N} \left\langle \sum_{i=1}^N \sum_{j \neq i}^N e^{-iq(r_i - r_j)} \right\rangle. \quad (31)$$

In a continuous medium, (31) can be written as:

$$S(q) = 1 + \frac{N-1}{V} \int_V g(r) e^{-iqr} dr, \quad (32)$$

where  $g(r)$  is the correlation function between particle mass centers. At  $q = 0$ , according to (31)  $S(q) = N$ .

We define the following function  $S_m(q)$  as

$$S_m(q) = S(q) - \frac{N-1}{V} \delta(q). \quad (33)$$

With  $\delta$  the Dirac function. Then,

$$S_m(q) = 1 + \frac{N-1}{V} \int_V [g(r) - 1] e^{-iqr} dr. \quad (34)$$

In the case of isotropic interactions, azimuthal (radial) averaging reduces (34) to:

$$S_m(q) = 1 + \frac{N-1}{V} \int_V 4\pi r^2 [g(r) - 1] \frac{\sin qr}{qr} dr. \quad (35)$$

To summarize, the intensity per unit volume  $V$  of  $N_p$  homogeneous isotropic scatterers of volume  $V_p$  and coherent length scattering density  $\rho_p$  dispersed in a medium of length scattering density  $\rho$  is the product of the form factor and the structure factor weighted by a contrast factor  $K_c$  follows:

$$I(q) = \Phi V_p \Delta \rho^2 P(q) S(q) = K_c P(q) S(q). \quad (36)$$

In the following, the three relevant parts of the above equation,  $\rho$ ,  $P(q)$ , and  $S(q)$  will be detailed and numerical applications will be described to aid in the understanding and interpretation of scattering curves.

## 5.2 SLD, Contrast Variation, and Isotopic Labeling

The SLD from a molecule with  $x_i$  atoms  $i$  and molecular volume  $v_p$  is:

$$\rho_p = \frac{\sum_i x_i b_i}{v_p} \quad (37)$$

$b_i$  is the coherent neutron scattering length of atom  $i$ . Only coherent scattered neutrons carry information about structure. The molecular volume  $v_p$  requires knowledge of the bulk density of the molecule. It can be difficult to measure and is a source of inaccuracy on the SLD value.  $\rho$  is usually expressed in  $\text{cm}^{-2}$  or  $\text{\AA}^{-2}$ .

The calculation of the atomic  $b_i$  is not trivial and values are experimentally determined and tabulated [20]. The magnitude is determined by the quantum mechanics of the neutron–nucleus interaction. It varies in an unsystematic way with the atomic number, depending on the direction of the nuclear spin and drastic variations can be found between two isotopes, the main example being the difference of value and sign between hydrogen and deuterium atoms. A negative value signifies a shift of  $\pi$  of the phase on scattering.

This last property is of great importance and opens the possibility of what is called “contrast variation.” The principle is to substitute one atom by one of its isotopes to induce a strong variation in the scattering length, assuming that no drastic perturbation of the properties (physical, chemical, etc.) of the sample occurs.

In soft condensed matter, the compounds of interest (colloids, emulsions, surfactants, polymers, etc.) contain a large quantity of hydrogen molecules which can be substituted in principle by deuterium atoms and  $b_H = -0.374 \cdot 10^{-12} \text{ cm}^{-2}$

and  $b_D = 6.37 \cdot 10^{-12} \text{ cm}^{-2}$ . This feature is at the origin of many SANS experiments and important advancements have been done in the description of molecular assemblies. One of the pioneering studies using the contrast variation method has been carried out by Stuhrmann in 1974 at the ILL [3–5] to investigate the structure of biological macromolecule like ferritin. In the first article the author concludes that “the most promising domain of neutron small-angle scattering seems to be the study of H-D exchange of reactions of macromolecules in dilute solutions.” Thirty years later, this conclusion is still relevant.

Isotopic substitution can be used to create a contrast inside a particle by a specific labeling of a part of the molecule. In the field of polymer science, the technique is widely used. For example, the difference in length scattering density between hydrogenated and deuterated polystyrene ( $\rho_{\text{PSH}} = 1.42 \times 10^{10} \text{ cm}^{-2}$  and  $\rho_{\text{PSD}} = 6.42 \times 10^{10} \text{ cm}^{-2}$ ) was used to follow the chain conformation during extrusion of a polymer melt made of a few percent (ca. 5%) of hydrogenated polystyrene mixed with deuterated polystyrene [15].

### 5.2.1 The Zero Average Contrast Method

For semidiluted polymer or polyelectrolyte solutions, both intra- and intercorrelations between the polymer chains contribute to the scattered intensity. The zero average contrast (ZAC) method allows the elimination of the signal coming from the structure factor (the intercorrelations) to see only the form factor from a single chain. The method consists in the exchange of hydrogen by deuterium atoms in the polymer chain and the modification of the length scattering density of solvent by a mixture of hydrogenated and deuterated molecules.

We consider a polymer solution containing  $N_h$  and  $N_d$ , H- and D-polymer chains, with  $N_h$  and  $N_d$  monomers, respectively. The volume fraction of deuterated monomers is called  $\Phi$ . The ZAC is obtained when the following condition is fulfilled:

$$(1 - \Phi)\Delta\rho_H + \Phi\Delta\rho_D = 0, \quad (38)$$

where  $\Delta\rho_H$  and  $\Delta\rho_D$  are the differences of length scattering densities from the H- and D- monomers and the solvent, respectively. Different examples of ZAC applications are illustrated by the references given in [27]. The experiments have demonstrated the vermicular form factors of fully charged PSSNa polymer chains. Reference [28] presents a study of polystyrene in diethylphalate in good solvent where the form factor of a single chain as a function of the shear rate is investigated.

## 5.2.2 Contrast Variation Technique

One of the main applications is found in multiple component systems to match a compound or a part of aggregate with a specific isotopic mixture of solvent. This technique called “contrast match” has been successfully used to elucidate the structure of particles composed of different layers, as for example, in microemulsions; to investigate surfactant layers adsorbed around mineral particles [29]; and for characterization of complex systems [30].

We recall that the scattered intensity for a dilute system without interaction is:

$$I(q) = \Phi V_p (\Delta\rho)^2 P(q). \quad (39)$$

At  $q = 0$ ,  $P(q)$  tends to 1 and

$$I(0) = \Phi V_p (\Delta\rho)^2 = \Phi V_p (\rho_p - \rho_s)^2. \quad (40)$$

$\rho_p$  is the average scattering density of the solute and  $\rho_s$  that of solvent or matrix.

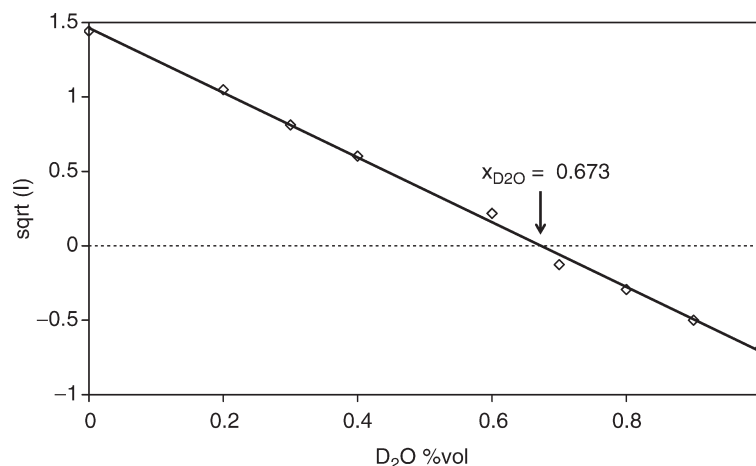
The knowledge of the molecular volume is sometimes a delicate point, and the calculation of  $\rho_p$  is extremely sensitive to  $V_p$ , the volume in bulk and thus to the density  $d$  since  $V_p = M/d$ ,  $M$  being the molar mass. In such cases  $d$  can be accurately determined by measuring the length scattering density of the molecule.

The average length scattering density of a H/D mixture is:

$$\bar{\rho}_s = x\rho_s^D + (1-x)\rho_s^H \quad (41)$$

with  $x$  the volume fraction of deuterated solvent.  $\sqrt{I(q \rightarrow 0)} \propto \pm(\Delta\rho)$  is linear as a function of  $x$  if the particles are monodisperse. At contrast match  $I(0) = 0$  one can deduce  $x$  and  $\rho_p$ . For polydisperse particles in solution, the intensity is never zero, and only a minimum is obtained.

Experimentally, a contrast variation experiment consists in measuring the scattered intensity at the lowest possible  $q$ . The samples prepared at the same concentration in different mixtures of D/H solvent, from fully deuterated to fully hydrogenated solvent. The following example presents an experimental determination of the SLD of laponite particles from a contrast variation experiment (Figure 13-10). Laponite is a synthetic clay which the particles have been characterized by other techniques as well (cryofracture and TEM [32]; AFM [31]). The particles can be described as monodisperse disks of 1 nm thickness and 30 nm diameter. The general composition is  $\text{Si}_8\text{Mg}_{5.45}\text{Li}_{0.4}\text{H}_4\text{O}_{24}\text{Na}_{0.7}$ , density 2.65, and the volume of the unit cell is  $4.7847 \cdot 10^{-22} \text{ cm}^3$ . One gets  $\rho_{\text{laponite}} = 3.94 \cdot 10^{10} \text{ cm}^{-2}$ .



■ **Figure 13-10**

Contrast variation experiment from an aqueous solution of Laponite,  $\Phi = 0.75\%$ . The square root of the absolute intensity at low  $q$  is plotted versus the volume fraction of D<sub>2</sub>O [31].

The contrast match point is found at volume fraction of D<sub>2</sub>O of 0.673, corresponding to  $\rho = 4.11 \cdot 10^{10} \text{ cm}^{-2}$ , in good agreement with the previously calculated value.

## 5.2.3 Contrast and Background

The contrast is strongly increased when one of the compounds (solvent or solute) is deuterated. Then one has to select a sample composition with fewer hydrogen molecules to reduce the incoherent background. In general, one chooses deuterated solvents because many of them can be purchased even if they remain expensive. On the other hand, deuterated molecules are less commonly used and require a good knowledge of chemistry to synthesize. Secondly, in dilute or semidilute solution, the main source of incoherent comes from the solvent.

## 5.2.4 Limits of Isotopic Labeling

In general, one assumes that there is no drastic change of the properties of the samples after isotopic substitution. Nevertheless, it is known that physical and chemical properties may slightly vary. The  $\theta$ -temperature, the melting

temperature, the temperature of phase transitions may change from few degrees. The CMC (critical micellar concentration) is decreased by replacing D<sub>2</sub>O by H<sub>2</sub>O. For example, the CMC of the nonionic surfactant C<sub>12</sub>E<sub>4</sub> varies from 4.91 10<sup>-5</sup> mol/L in H<sub>2</sub>O to 5.65 10<sup>-5</sup> mol/L in D<sub>2</sub>O at 25°C [33].

Phase separation has been observed in binary mixtures of deuterated and hydrogenated polymer as mentioned in [34] with polybutadiene and can lead to incorrect interpretations of sample behavior if extrapolated to fully protonated samples.

A significant  $q$ -dependence has been measured in hydrogenated and deuterated mixtures of alkanes ( $n$ -decane and isooctane) whereas the scattering of pure hydrogenated and deuterated solvent gives flat isotropic scattering. Alkane molecules are relatively large and there is no exchange of H and D as in light and heavy water mixtures. Consequently, there is a coherent term resulting from the sum of scattering due to density and composition fluctuations [35].

Labile hydrogens from alcohol, acid or base functions can be exchanged between solute and solvent. They have to be taken into account in contrast match experiments. Examples of length scattering variations for various amino acids in D<sub>2</sub>O/H<sub>2</sub>O mixtures are plotted in [36].

### 5.3 Analytical Expressions of Particle Form Factors

Two possible approaches may be applied to determine the particle form factor. The direct method consists in calculating analytical expressions which are compared to the experimental data by varying parameters (radius, length, polydispersity, etc) in order to minimize the  $\chi^2$ :

$$\chi^2 = \sum_{N-x} [(I_{\text{model}}(q) - I_{\text{exp}}(q))/E(q)]^2 / (N - x). \quad (42)$$

$E(q)$  is the error on experimental intensity;  $x$  is the number of variables.

In most of the cases, when no interaction peak is present, the intensity falls quickly with  $q$ . Equation (36) assigns a larger weight to the accurate agreement between experiment and model at low  $q$  values. Taking the logarithm of the intensity will enhance the weight of points at high  $q$  and improve the fitting at large angles.

The indirect methods treat the inverse Fourier transform of the data. A detailed review of particle form factors can be found in [37]. In the following, only the most used equations are recalled and illustrated by typical selected examples, the following list is of course not exhaustive.

### 5.3.1 Sphere

The form factor of homogeneous sphere of radius  $R$  is known since 1951 [38]:

$$F_S(q, R) = \left[ 3 \frac{\sin(qR) - (qR) \cos(qR)}{(qR)^3} \right] \text{ and } P_S(q, R) = [F_S(q, R)]^2. \quad (43)$$

The  $P(q)$  of the sphere is equal to zero for  $qR = 4.493, 7.725$ , etc.

This form factor can be applied to describe surfactant micelles in solution, colloidal particles (latex, ferrofluid, silica beads), or globular protein in biology.

### 5.3.2 Concentric Shells and Hollow Sphere

The case of sphere can be extended to spherical concentric shells.  $N$  shells are considered, with radii  $R_i$  and scattering densities  $\rho_i$ ,  $R_1$  being the outer radius, then:

$$P(q) = F^2(q) = \left[ \sum_{i=1}^N V_i (\rho_{i-1} - \rho_i) F_S(q, R_i) \right]^2, \quad \rho_0 = \rho_s, \text{ the solvent SLD.} \quad (44)$$

In the case of two concentric shells of radii  $R_1$  and  $R_2$ ,  $R_1 > R_2$ , the previous equation is reduced to:

$$P(q) = F^2(q) = \left[ \frac{(\rho_1 - \rho_s) V_1 F_S(q, R_1) + (\rho_2 - \rho_1) V_2 F_S(q, R_2)}{(\rho_1 - \rho_s) V_1 + (\rho_2 - \rho_1) V_2} \right]^2. \quad (45)$$

The core-shell model describes accurately colloidal particles composed of a core and a shell. An example combining SAXS and SANS can be found in [39], where PNIPA chains are grafted on a solid poly(styrene) core.

Even if a single spherical model gives reasonable fittings in many systems like micelles in solution, the data fitting is considerably improved by the use of a two-shell model. Indeed, due to hydration of the polar heads, the length scattering densities of the core and of the hydrophilic parts are significantly different. A recent article deals with the modeling of core-shell spherical micelles made of the ionic surfactant (or small polymer)  $C_{18}E_{100}$ , which possesses a huge head group in comparison with the hydrophobic core [40]. A detailed model for the scattering intensity is developed there. Instead of a two-shell model, the authors add to the classical form factor from a sphere a smoothly decaying scattering density at the surface, a more realistic model, to represent roughness between core and shell and water penetration in the first Angstroms of the hydrophilic part.



Taking  $\rho_2 = \rho_s$ , the last equation represents a hollow sphere with an envelop thickness of  $R_1 - R_2$ .

$$P(q) = F^2(q) = \left[ \frac{(\rho_1 - \rho_s)}{V_1 - V_2} (V_1 F_S(q, R_1) - V_2 F_S(q, R_2)) \right]^2. \quad (46)$$

This model can describe, for example, the scattering of vesicles (liposomes). Many examples are found in literature due to the increased interest of such assemblies which may mimic biomembranes.

Another example of an application of this equation is found for microemulsion. In oil in water emulsions, oil droplets are dispersed in a continuous medium of water, the interface between the two media is composed of a monolayer of surfactant molecules. The SLD profile exhibits three steps. By contrast variation experiments, it is then possible to match the surfactant layer or on the contrary to only see it. An illustration can be seen in [41] with the ternary system AOT/Water/Decane.

### 5.3.3 Cylinder

The expression for a cylinder with radius  $R$  and length  $2L$  was calculated in 1951 by Fournet [42]

$$P(q) = \int_0^{\pi/2} \frac{\sin^2(qL \cos \alpha)}{(qL \cos \alpha)^2} \frac{4J_1^2(qr \sin \alpha)}{(qr \sin \alpha)^2} \sin \alpha d\alpha. \quad (47)$$

$\alpha$  is the angle between the normal to the particle and the scattering vector  $q$ .  $J_1$  is the first order Bessel function. Below  $q = \pi/R$ , the  $P(q)$  reaches a plateau. For highly asymmetrical particles, with  $e/R \ll 1$ , and  $q > \pi/R$ , the scattering intensity decreases as  $q^{-2}$ . The minima of the function are found for  $qR = 3.83, 7.01$ , etc.

Catanionic mixtures of surfactants exhibit rich phase diagrams, where vesicles, elongated and flat micelles, or lamellar phases are formed as a function of the surfactant composition. An example of cylindrical micelles formed by catanionic surfactants in water can be found in [43]. Flat rigid nanodisks have been reported in [44], where the SANS curves exhibit a  $q^{-2}$  decrease over more than two decades. Flat rigid particles as clay (laponite) are also well-fitted by equation (47) [32, Mourchid et al.].

### 5.3.4 Ellipsoid

Let us consider an ellipsoid of revolution with semi-axis  $R$ ,  $R$ , and  $\epsilon R$ . The expression calculated by Guinier [1] is:

$$P(q, R, \varepsilon) = \int_0^{\pi/2} P_s(q, r(R, \varepsilon, \alpha)) \sin \alpha d\alpha \text{ with } r(R, \varepsilon, \alpha) = R\sqrt{\sin^2 \alpha + \varepsilon^2 \cos^2 \alpha}. \quad (48)$$

$P_s$  is the form factor from a sphere (43). Oblate or prolate ellipsoidal objects are easily formed by nonionic surfactant micelles [45]. The mixture of different surfactant or the addition of host molecules can induce a change in shape from sphere to ellipsoid due to modifications of interactions between surfactant head groups [46]. Another example is the polymerization of styrene in vesicle bilayer which creates oblate particles, clearly visible by SANS experiments [47].

### 5.3.5 The Guinier Approximation

When  $q$  tends to 0, in the range where  $qR < 1$ , Guinier has shown that  $P(q)$  has a general form which depends only on the radius of gyration of the particle  $R_g$ :

$$P(q) = \Phi V_p \left[ 1 - \frac{(qR_g)^2}{3} + \dots \right] \approx \Phi V_p \exp \left( -\frac{(qR_g)^2}{3} \right). \quad (49)$$

This powerful approximation allows one to obtain geometric information by looking only at the behavior at small angles. Nevertheless one should keep in mind that it is only valid at  $qR < 1$  for systems without interactions. The plot of  $\ln(I)$  as a function of  $q^2$  gives a linear function, where  $R_g^2$  is given by the slope.

### 5.3.6 The Zimm Approximation

For macromolecules in solution, an often used approximation, also coming from limited development of  $I(q)$ , is the Zimm's approximation:

$$\frac{c}{I(q)} = \frac{1}{I_0} \left( 1 + \frac{(qR_g)^2}{3} \right). \quad (50)$$

### 5.3.7 Fractals

One of the most beautiful examples of a fractal in everyday life is the Romanesco cabbage (► *Figure 13-11*). Fractals are defined by a self-similar structure in a given



■ Figure 13-11

The Romanesco cabbage: a natural example of a volume fractal

spatial range where the shape observed is independent from the length scale. The mass  $M$  in a volume  $R^d$  follows the power law  $M(R) \propto R^D$ ,  $D$  is called the fractal dimension. The density of matter at a distance  $R$  from any subunit center varies as

$$\rho(R) \propto R^{D-d}. \quad (51)$$

By Fourier transform one gets

$$I(q) \propto q^D. \quad (52)$$

Mass fractals are characterized by exponent between 1 and 3 and surface fractals by exponents between 3 and 4. If mathematically the fractal behavior extends to all length scales, in practice it stops at small scales when the individual scatterers are seen and at large scales when the process of growth stops. In a log–log scale representation, the slope gives directly the fractal dimension and must be observed at least in one order of magnitude to deduce with certitude a fractal process.

### 5.3.8 Concentrated Surfactant Phases

Surfactant molecules are widely used and studied in soft condensed matter. They are at the base of membrane cells and are found nearly everywhere in everyday life, either as natural or synthetic molecules in food, cosmetic, cleaning, ink, etc. If in industry they are used mainly in dilute conditions, these amphiphilic molecules with a hydrophilic head and a hydrophobic core form various shapes and organizations in water or oil in more concentrated states. Micelles are

generally formed at low concentrations. At higher concentrations, or in presence of salt or by varying the temperature, lamellar, sponge, cubic, or hexagonal phases are formed. All of these phases give typical patterns, where the form factor is modulated by the structure factor. In concentrated and well-ordered systems several Bragg peaks can be measured (see for example, [Figure 13-13](#)). From their shape and size, the bending modulus and the rigidity of membranes can be extracted. For interested readers the following articles and lectures are recommended [45, 46].

### 5.3.9 Case of Polymers

SANS experiments have greatly contributed to a deeper understanding of the phase behavior and the structure of polymer melts and solutions. Please refer to the articles published in this book from G. Berry (vol I, chap 2), C. Giacomeli and R. Borsali (vol I, chap 3), S. Pederson (vol I, chap 4), Y. Nakamaru/Norisuye (vol I, chap 5), I. Hamley & V. Castelletto (vol II, chap 8).

### 5.3.10 Case of Interfaces

We consider a two-phase system. At large  $q$  vectors, the interface is observed at a small scale. Now if the scattering vector is much larger than the characteristic curvature of the interfaces, they appear flat and the intensity is proportional to the total surface area  $\Sigma$ , independently of the shape of the two phases.

The so-called Porod limit (1951) says that for a sharp interface (in the normal direction but smooth in any parallel direction) the intensity decreases as  $q^{-4}$  at large  $q$  as

$$\Sigma = \frac{1}{2\pi(\Delta\rho^2)} \lim_{q \rightarrow \infty} I(q)q^4, \quad (53)$$

where  $\Sigma$  is the specific area, i.e, the surface developed by the interface per unit volume in  $\text{m}^2/\text{m}^3$ .

Assuming a spherical geometry of the particles, the radius can be deduced as:

$$R = \frac{3\Phi}{\Sigma}. \quad (54)$$

In the case of particles of typical size  $R$ , measuring in the Porod limit means that the  $q$ -range has to be extended up to  $qR = 10$ .

A precise determination of the specific area is closely related to the precision of the absolute scaling. The equation allows one to determine the size of very large particles up to the order of micrometers.

An example of an application is the measurement of the droplet size in the spontaneous emulsion formed by the well-known beverage “Pastis” [50]. The emulsion is formed by anethol droplets in a continuous medium of water and ethanol. The radius of droplets is of the order of micrometers and increases with time and temperature. Even on D22, the complete form factor is not accessible by SANS. Only the last part of the form factor, decreasing as  $q^{-4}$  is viewed and from this discrepancy it is possible to deduce the radii of the particles.

The porod law has been used to analyze data from mesoporous materials (or cement), which develop a large interface with closed pores not accessible with other techniques (as gaseous absorption, for example). Other applications concern pores in alumine [51], surfactant phases [52], gels [53], or emulsions [54].

Correction of the Porod limit becomes necessary when the modulus of the scattering vector is of the same order as the surface curvature (surface roughness). Different corrections are detailed in [55].

The different form factors (sphere, hollow sphere, ellipsoid, cylinder, and disk) are illustrated in [Figure 13-12a](#) and [b](#). The calculation is done for radius or length of 150 Å and layer thickness of 20 Å, in order to compare for identical parameters the variation of the scattering curves induced by the different shapes. The ellipsoidal shape is calculated for  $R = 150$  Å and  $\varepsilon = 3$ . For a more realistic representation, the form factors are smeared by a log-normal polydispersity function, as will be explained in the next section. The log-log representation puts clearly into evidence different regimes. At low  $q$ , for  $qR < 1$ , the scattering curves reach a plateau and are in the so-called “Guinier” regime. Then the first oscillation is related to the larger dimension of the scatterers (outer radius, cylinder length, etc.). At intermediary range, the double logarithmic representation appears as a linear slope which is related to the aggregate shape:

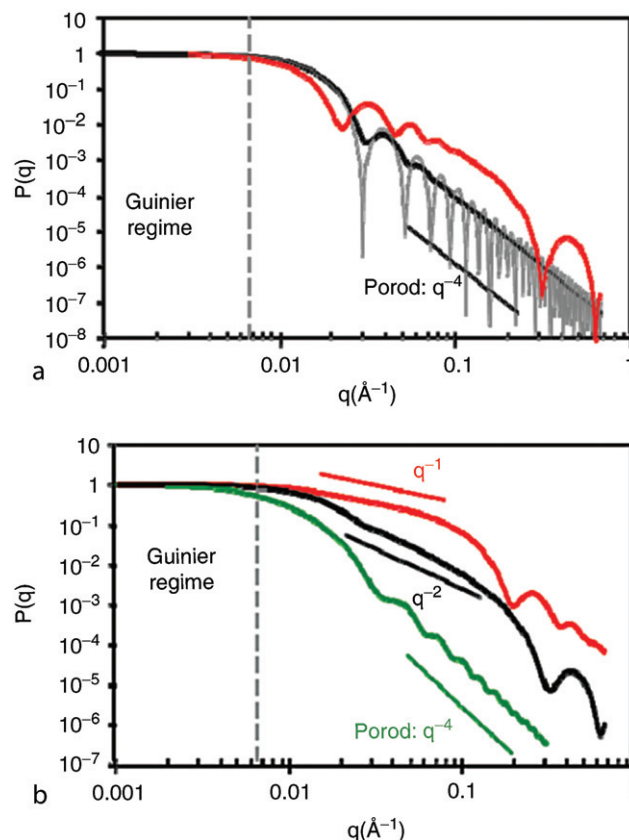
$q^{-1}$  slope: 1D object like rigid fibers.

$q^{-2}$  slope: 2D object or locally planar, as for example, membrane, flat colloidal particle.

At high  $q$ , the minimum of the oscillation is related to the lowest dimension of the objects (vesicle bilayer, disk thickness, etc.), followed by a  $q^{-4}$  slope, characteristic of the interface between the objects and the solvent.

## 5.4 Indirect Fourier Transform Method

The following method has been developed by O. Glatter. The details of calculation are explained in journal articles [56] and in a book of lecture notes [57]. In this approach, there is no hypothesis a priori on the size, shape, and polydispersity of the scattered objects. It consists of an inverse Fourier transformation of the



■ **Figure 13-12**

Comparison of form factors. Figure 12 (a) sphere (grey) smeared with a function of polydispersity (grey), hollow sphere (red); Figure 12 (b) ellipsoid (green), disk (black) and cylinder (red)

experimental scattering curves which yields the pair distance distribution function  $p(r)$ . The PDDF gives information of the structure in the real space and needs to be compared with calculated models, as spheres, cylinders, etc.

It is also possible to construct a model based on an analytical form for the objects with complex shapes and inhomogeneous density. The validity of the model is tested by calculation of the PDDF and  $I(q)$  and comparison with the experimental data. Every model that can fit within the errors is acceptable. Additional parameters (obtained with other techniques) will be needed to select the right model.

More recently, the generalized indirect Fourier transform (GIFT) aims to determine simultaneously the form factor and the structure factor in case of interacting particles [58]. The pertinent use of the program package requires training; it is then an extremely powerful tool for SANS data analysis.

Ab initio analysis of particle shape and domain structure programs has been developed by D. Svergun as well. The approach based on IFT is explained in detail in [59]. The powerful algorithms are used in soft condensed matter but also for biological samples, as for example, to refine the configuration of proteins in solutions.

## 5.5 Structure Factors of Colloids

A detailed lecture on interacting colloidal suspensions can be found in [60].  $S(q)$  is related to the pair correlation function  $g(r)$ , which describes the local order of the scatterers, i.e., the probability of finding a particle at a given distance from another one.  $g(r)$  depends on the interaction potential.

$$g(r) = e^{-\frac{V(r)}{k_B T}}, \quad (55)$$

where  $V(r)$  is the mean field potential. In case of relatively dilute systems,  $V(r) = U(r)$ , the interaction pair potential.

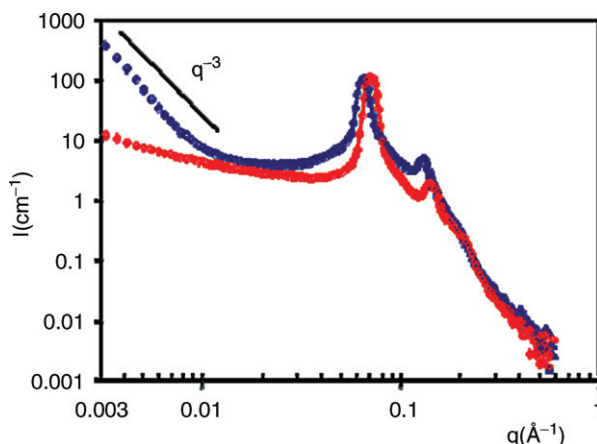
Assuming that  $N > 1$ , the structure factor can be written as

$$S(q) = 1 + \frac{N}{V} \int_V (g(r) - 1) e^{-iqr} dr. \quad (56)$$

Or in case of isotropic interactions (56) becomes

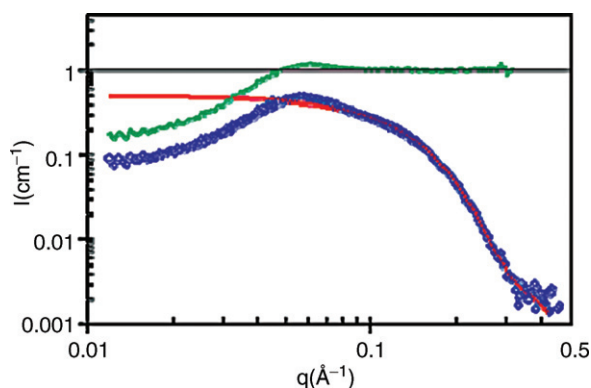
$$S(q) = 1 + 4\pi \frac{N}{V} \int_V (g(r) - 1) r^2 \frac{\sin qr}{qr} dr. \quad (57)$$

Typically, the structure factor is a dimensionless oscillatory function that tends to unity at high  $q$  and equals 1 for dilute solutions. The first maximum at  $q_0$  is related to the distance between the nearest neighbors by  $2\pi/q_0$ . The experimental structure factors can be obtained by measuring the absolute intensity at two particle concentrations and by dividing the scattering at the highest concentration by the one at lowest concentration, in dilute condition. The resulting curve can be then compared with existing models, trying different pair potential. Attractive interactions or biphasic samples induce an increase of the intensity at low  $q$ , whereas a decrease of the intensity is the signature of repulsive interactions. In [Figure 13-13](#) an example of aggregation and attractive interaction in lamellar phase is presented. The lamellar  $L_\alpha$  phase is made by dilution in  $D_2O$  of AOT, an anionic surfactant with  $C_{12}E_4$ , a nonionic surfactant (molar surfactant ratio 1:1). For a total volume fraction of surfactant of 24%, micelles and  $L_\alpha$  are in osmotic equilibrium, the sample is slightly turbid and a  $q^{-3}$  upturn is observed at low  $q$ . As soon as the single-phase regime is reached, the low  $q$  intensity strongly



■ Figure 13-13

Lamellar phases made by mixing charged (AOT) and uncharged ( $C_{12}E_4$ ) surfactant molecules [28]. The molar ratio between AOT and  $C_{12}E_4$  is.  $\Phi$  is the total volume fraction of surfactant in  $D_2O$ . ( $\diamond$ )  $\Phi = 24\%$ , ( $\circ$ )  $\Phi = 30\%$ . The strong increase of the intensity as a  $q^{-3}$  slope is characteristic from a biphasic sample



■ Figure 13-14

Scattering from AOT micelles,  $\Phi = 1\%$ . ( $\diamond$ ) Experimental points; (—) Best-fit obtained using the form factor of ellipsoid (48),  $R = 15.7 \text{ \AA}$ ,  $\varepsilon = 1.15$ ; (—) Experimental structure factor obtained by dividing the experimental scattering form by the fitted form factor. The lowering of the intensity traduces repulsive interactions and the peak position is related to the mean distance between micelles

decreases. On the other hand, in [Figure 13-14](#), the lowering of the low  $q$  intensity is due to the repulsive interaction between charged micelles. The red curve represents the fitted form factor and the green one is the experimental structure factor.



Most of the expressions are calculated in the frame of statistical mechanics and liquid state theory for particles with spherical symmetry and interacting with a symmetric potential. The pair correlation function  $g(r)$  is calculated by means of the Ornstein–Zernike integral equations with an additional equation known as the closure equation to describe the pair potential of the system under investigation.

The wide variety of colloids yields to very different kind of interactions from hard sphere to long-range soft potentials. There are only few cases where an analytical expression exists. For all the others, numerical calculations need to be performed.

For hard-sphere systems, the expression is calculated with the Percus–Yevick approximation for the closure relation. The system is fully described by the hard sphere radius and volume ( $R_{SH}$  and  $\Phi_{SH}$ ) [61].

A widely used analytic expression for charged colloids in a repulsive screened Coulomb potential has been given by Hayter and Penfold in 1981, where the OZ equation is solved in the Mean Spherical Approximation theory (MSA) [62]. The equations are mainly valid in the case of relatively high colloid concentrations. In 1982, the model has been extended to dilute systems. The new closure equation is known as the “Rescaled Mean Spherical Approximation” (RMSA) [63].

The model has been successfully applied for charged micelles or colloids. The variable parameters are the ionic strength ( $c_s$ ), the volume fraction ( $\Phi$ ), the colloid charge ( $\sigma$ ), and the radius ( $R$ ). Some of these parameters are known from the sample preparation ( $c_s$ ,  $\Phi$ ). In many cases, the radius can be extracted from the form factor. Then structure factor fitting allows one to estimate the rate of counter-ion dissociation or the screening length, for example. Important progresses in the understanding of counter-ion role have been so realized and compared to behavior described by the Hofmeister series.

## 6 Instrument Resolution and Polydispersity

In the latter chapter, ideal form factors have been presented. However, in most of the cases, these form factors do not fit the experimental data as well as expected. Instrument resolution and polydispersity of the scatterers have to be introduced in the model [64, 65]. Here, the effect of instrumental resolution and polydispersity will be compared.

To illustrate the effects, the model of a spherical shell is used: the outer radius  $R_1$  is fixed at 220 Å and layer thickness at 20 Å (45).  $\Delta\rho$  is set at 1 so that  $P(0) = 1$ . A background of  $10^{-3}$  is added to cut the very deep oscillations at large  $q$  (down

to  $10^{-8}$ ), to reduce the amplitude of the intensity axis and to see better the differences between the simulations.

The resolution is the uncertainty of the measured  $q$  value and indicates the possibility to resolve sharp features such as oscillations or Bragg peaks. As shown below,  $\Delta q/q$  depends partially on the wavelength spread, which is quite different between time-of-flight and steady-state instruments. The following considers only the latter kind of instruments. Resolution calculation for time-of-flight spectrometers is detailed in [66].

The smearing of the ideal scattered intensity has three factors: the finite size of the incident beam, the wavelength resolution, and the pixel size on the detector [65]. Only the first two points will be considered since the pixel size (max  $10 \times 10 \text{ mm}^2$ ) has a negligible effect.

The  $q$ -resolution at a given  $q$  may be written according to a Taylor expansion as:

$$\Delta q = -q \left( \frac{\delta \lambda}{\lambda} \right) + \left( \frac{4\pi}{\lambda} \right) \cos \theta \Delta \theta. \quad (58)$$

Hence,

$$\begin{aligned} \Delta q^2 &= q^2 \left( \frac{\delta \lambda}{\lambda} \right)^2 + \left( \frac{4\pi}{\lambda} \right)^2 \cos^2 \theta \Delta \theta^2 = \Delta q^2(\lambda) + \Delta q^2(\theta) \\ &= q^2 \left[ \left( \frac{1}{2\sqrt{2} \ln 2} \frac{\Delta \lambda}{\lambda} \right)^2 \right] + \left[ \left( \frac{4\pi}{\lambda} \right)^2 - q^2 \right] \Delta \theta^2. \end{aligned} \quad (59)$$

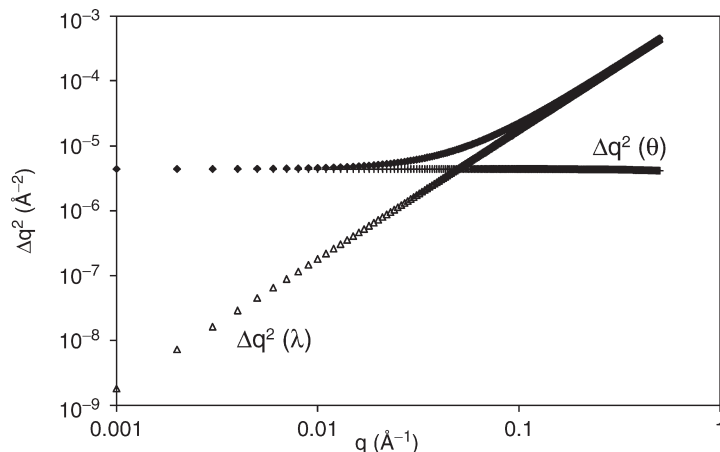
$\Delta \lambda/\lambda$  is related to the FWHM (full width at half maximum) value of the triangular function describing the wavelength distribution by  $\text{FWHM} = \lambda_0 (\Delta \lambda/\lambda)$ .  $\Delta \theta$  is related the width of the direct beam (► *Figure 13-15*). A detailed description of  $\Delta \lambda/\lambda$  ( $\delta \lambda/\lambda$ ) and  $\Delta \theta$  is given in Appendix (6.7).

From (59), one can see clearly that  $\Delta q^2$  depends on the wavelength spread and also on  $q$  value. The contribution from  $\Delta \theta$  is quasi-constant versus  $q$ , the one from  $\lambda$  increases with  $q$ . At low  $q$  ( $< 10^{-2} \text{ \AA}^{-1}$ ), the uncertainty is dominated by the distribution in angle. At large  $q$ -values,  $\Delta q$  is due to the wavelength spread.

The resolution function  $R(q', q, \Delta q)$  describes the distribution of the  $q$  vectors at a given instrumental configuration. The experimental intensity  $I_{\text{exp}}$  is the real intensity scattered by the sample  $K_c F^2(q, r_o)$  (36) smeared by the resolution function  $R(q', q, \Delta q)$ :

$$I_{\text{exp}}(q) = \int_{q' - \infty}^{q' + \infty} R(q', q, \Delta q) I(q') dq'. \quad (60)$$

Assuming a Gaussian function for the resolution, (60) yields:



■ Figure 13-15

Contributions of  $\Delta \lambda/\lambda$  ( $\Delta$ ),  $\Delta \theta$  (+) to the total  $q$ -distribution,  $\Delta q^2$  ( $\diamond$ ). Curves are calculated for  $\lambda = 6 \text{ \AA}$ ,  $\Delta \lambda/\lambda = 10\%$ , and  $\Delta \theta = 10^{-3} \text{ rad}$

$$I_{\text{exp}}(q) = \int_{q' \rightarrow -\infty}^{q' \rightarrow +\infty} \frac{1}{\Delta q \sqrt{2\pi}} \exp\left(-\frac{(q' - q)^2}{2(\Delta q)^2}\right) I(q) dq'. \quad (61)$$

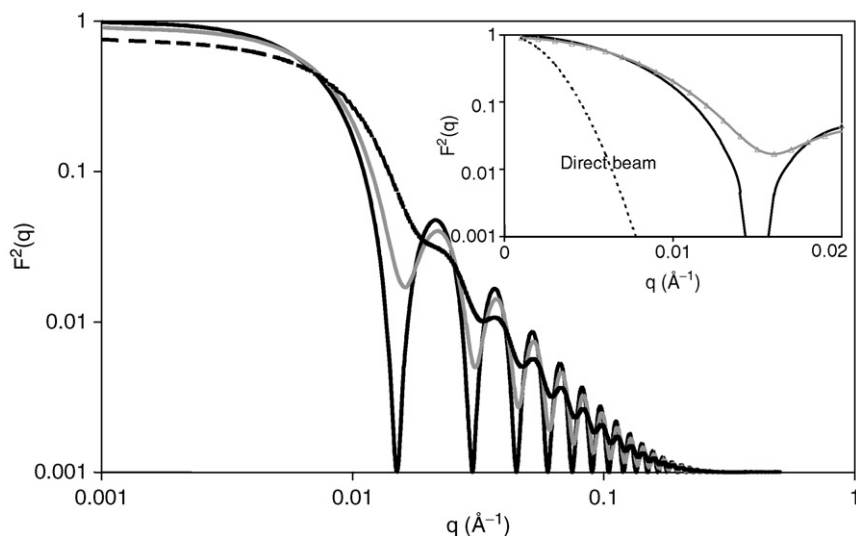
In practice, the range of integration  $q' - \infty$ ,  $q' + \infty$  is replaced by  $q' - a$ ,  $q' + a$  where  $a$  depends on the width of the Gaussian function, i.e., on  $\Delta q^2$ . The higher  $\Delta q^2$ , the larger is the integration range which has to be used. A too small integration range would yield to an underestimation of the smearing, particularly at high  $q$ , where the function is broader.

## 6.1 Effect of the Beam Divergence and Size: $\theta$ Resolution

As shown in (76),  $\Delta \theta$  varies between  $8 \times 10^{-4}$  and  $2.6 \times 10^{-3} \text{ rad}$  on D22. These smearing effects are presented in Figure 13-16. In insert, a zoom of the low  $q$  region is presented; the direct beam width is compared to the width of the first oscillation of the ideal form factor and the resulting smeared curve is drawn. The direct beam size has a large influence at small angles inducing an intensity decrease of the plateau and smoothing the first oscillations with a shift of the minima toward higher  $q$ .

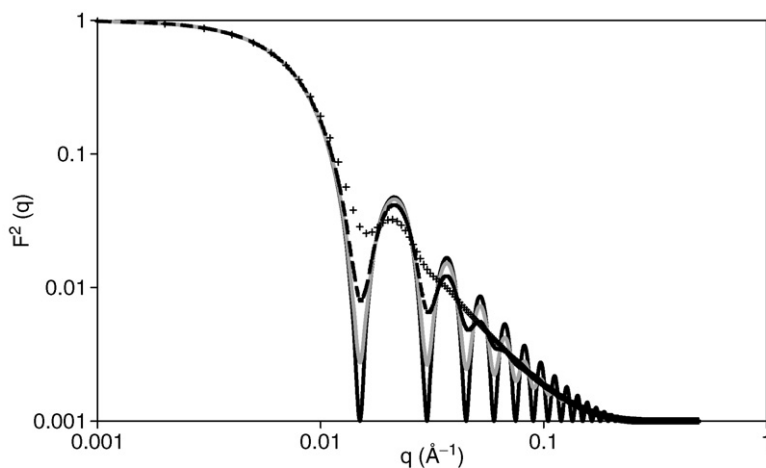
## 6.2 Effect of the $\lambda$ Distribution

In Figure 13-17, one sees that on such a sample, the effects are most noticeable for  $\Delta \lambda/\lambda > 20\%$ . Above this value, the oscillations vanish. Below 20%, the



■ Figure 13-16

Effect of the  $\Delta\theta$  on the ideal scattering of a monodisperse spherical shell,  $R_2 = 200 \text{ \AA}$ ,  $\lambda = 6 \text{ \AA}$ ,  $\Delta\lambda/\lambda = 0$ . (—)  $\Delta\theta = 0$  rad; (—)  $\Delta\theta = 1 \times 10^{-3}$  rad corresponding to  $\Delta q(0) = 2.0 \times 10^{-3} \text{ \AA}^{-1}$ ; (.....)  $\Delta\theta = 2 \times 10^{-3}$  rad corresponding to  $\Delta q(0) = 4.2 \times 10^{-3} \text{ \AA}^{-1}$ . In insert, comparison of the direct beam width (....)  $\Delta\theta = 1 \times 10^{-3}$  rad ( $\Delta q(0) = 2.1 \times 10^{-3} \text{ \AA}^{-1}$ ) with the width of the first oscillation of the form factor, (—)  $\Delta\theta = 0$  and the resulting smeared curve (—)  $\Delta\theta = 1 \times 10^{-3}$  rad. Curves plotted in semi-log scale



■ Figure 13-17

Effect of the wavelength resolution on the ideal scattering of a monodisperse spherical shell,  $R_2 = 200 \text{ \AA}$ ,  $\lambda = 6 \text{ \AA}$  and  $\Delta\lambda = 0$ . (—)  $\Delta\lambda/\lambda = 0$ ; (—)  $\Delta\lambda/\lambda = 10\%$ ; (...)  $\Delta\lambda/\lambda = 20\%$ , and (+)  $\Delta\lambda/\lambda = 40\%$

oscillations are still visible but a broadening is observed. In contrast with the  $\theta$ -resolution, the smearing effects by  $\lambda$  are important at large  $q$ .

## 6.3 Smearing Examples

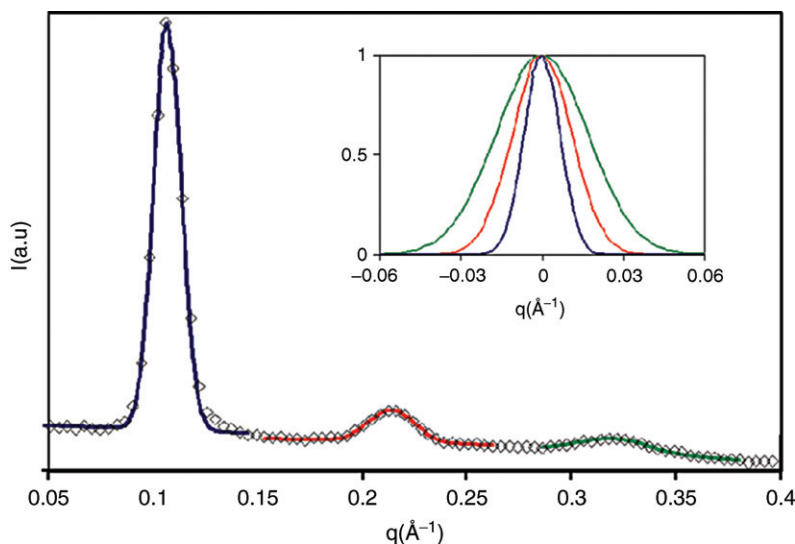
### 6.3.1 Evidence of Wavelength Spread on Bragg Peaks

A simple and easy experiment to demonstrate the wavelength spread is to use a polycrystalline sample, giving narrow Bragg peaks, with several orders at large angles ( $>0.1 \text{ \AA}^{-1}$ ). For example, tetradecanol, octadecanol [67], or silver behenate [68] are currently used for  $q$ -range calibration and give their first order Bragg peak at  $q_b = 0.1583, 0.1521$ , and  $0.10763 \text{ \AA}^{-1}$ , respectively.

In this range of  $q$  larger than  $0.1 \text{ \AA}^{-1}$  the uncertainty in  $q$  is mainly governed by the wavelength spread (► Figure 13-15). At the position of  $n^{\text{th}}$  Bragg peak, (59) becomes:

$$\Delta q_b^{n2} = n^2 \Delta q_b^2(\lambda) + \Delta q_b^{n2}(\theta). \quad (62)$$

For this experiment silver behenate was used. Silver behenate was purchased from Johnson Matthey chemicals and used without further treatment, but kept in a dry dark place. Three wavelengths 6, 8, and  $10 \text{ \AA}$  have been used. In ► Figure 13-18,



■ Figure 13-18

Scattering curve of silver behenate. In insert, the three Bragg peaks are normalized  $\sigma 1$  in intensity to evidence the enlargement of the peaks due to the wavelength spread

the scattering curve obtained at  $\lambda = 6 \text{ \AA}$ ,  $D = 2 \text{ m}$ , and  $C = 14.4 \text{ m}$  is presented. Three Bragg peaks are visible. In insert, the width of the peaks normalized  $\sigma$  1 in intensity is compared.

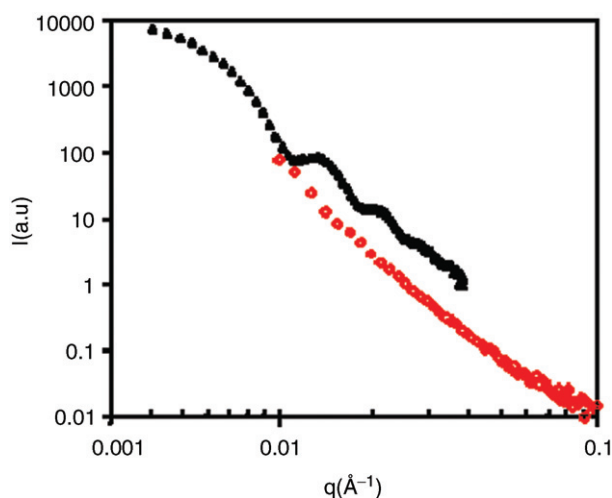
The Bragg peaks are fitted with a Gaussian function given  $(\Delta q_b^n)_{\text{exp}}$  equals to 0.0066, 0.011, 0.017  $\text{\AA}^{-2}$  for  $n = 1, 2$ , and 3, respectively. A full series of measurements at different wavelengths and collimations and calculation details are presented in [69].

In powder diffraction, the width of the Bragg peak and the enlargement is related to the mosaicity. In soft condensed matter for lamellar phases, the Bragg peak shape is related to bending constant and elasticity of bilayer. The presented example shows the importance of the knowledge of the instrument resolution for accurate determination of parameters.

Inversely, a well-known crystal with a very small mosaicity giving sharp Bragg peaks can be used to determine the wavelength spread.

### 6.3.2 Importance of the Choice of Instrument Configurations

The choice of instrument configuration can strongly affect the data analysis. An example is given in [Figure 13-19](#). Calibrated monodisperse latex particles were purchased by Aldrich (ref cat 46,169-5,  $R = 430 \text{ \AA}$ ,  $\sigma = 0.006$ , size determined by



■ Figure 13-19

Scattering of monodisperse spheres of latex at two configurations.  $\lambda = 6 \text{ \AA}$ , ( $\Delta$ ),  $D = 17.6 \text{ m}$  and  $C = 17.6 \text{ m}$ , ( $\diamond$ ),  $D = 5.6 \text{ m}$  and  $C = 5.6 \text{ m}$

TEM measurements by Aldrich) and used as received. The two instrument configurations used optimize the flux at the sample position:  $D = 17.6$  and  $C = 17.6$  m for the low angles and  $D = 5.6$  and  $C = 5.6$  m, with a wavelength  $\lambda = 6$  Å. The scattering curves are shifted of a factor of 5 in intensity. The form factor oscillations are clearly visible in the low  $q$  configuration, whereas, they are totally smeared in the other configuration where only the curve envelop is seen. In such case, data fitting gives very large uncertainty on the radius, around 40% and sometimes never converges.

## 6.4 Polydispersity

Most colloidal suspensions are composed of polydisperse objects. The form factor of monodisperse particles  $F^2(q, R_2)$  is smeared with the size distribution function  $G(R_2, r, x)$ , where  $x$  is the parameter characterizing the width of the distribution:

$$I_{\text{poly}}(q, R_2) = \int_0^\infty G(R_2, r, x) I(q, r_2) dr. \quad (63)$$

Gaussian, log-normal functions or Schultz distribution are often used to represent the size spread, around an average value  $R_2$ . The normalized expressions ( $\int_0^\infty G(r) dr = 1$ ) are given here; their shapes and principal properties are compared in [Figure 13-20](#).

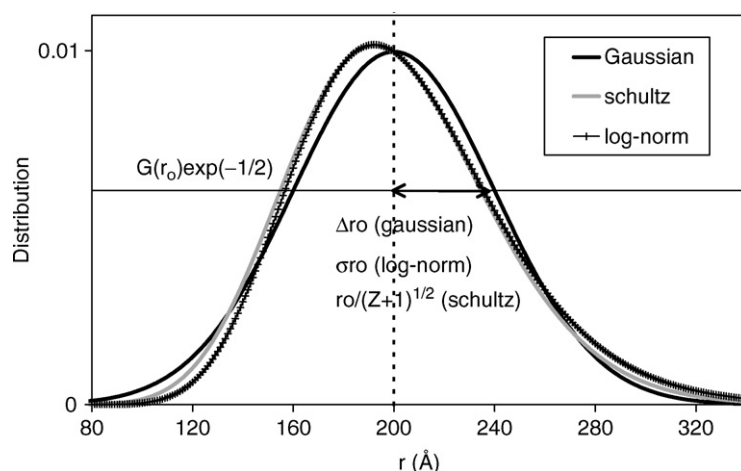


**Figure 13-20**

Comparison of the three size distribution laws.  $R_2 = 200$  Å;  $\Delta r_0 = 40$  Å (gaussian);  $\sigma_r = 0.2$  (log-normal), and  $Z = 90$  (Schultz)

- The Gaussian function is:

$$G_G(R_2, r, \Delta R_2) = \frac{1}{\Delta R_2 \sqrt{2\pi}} \exp\left(-\frac{(r - R_2)^2}{2\Delta R_2^2}\right), \quad (64)$$

where  $\Delta R_2$  is the half-width of the Gaussian function for  $G_G(R_2, R_2 + \Delta R_2) = G(R_2) \exp(-1/2) = 0.606$ . The Gaussian function is symmetric about its maximum  $R_2$ .

- The log-normal distribution is equal to:

$$G_{LN}(R_2, r, \sigma_0) = \frac{1}{r \sigma_0 \sqrt{2\pi}} \exp\left(-\frac{1}{2\sigma_0^2} \left(\ln \frac{R_2}{r}\right)^2\right), \quad (65)$$

$\sigma_0$  is the standard mean deviation, related to the half-width by  $\Delta r_0 = \sigma_0 r_0$ . The maximum of the function is found for  $r = r_0 \exp(-\sigma_0^2)$ .

- The Schultz distribution is:

$$G_S(R_2, r, Z) = \left(\frac{Z+1}{R_2}\right)^{Z+1} \exp(-R_2 r) / \Gamma(Z+1), \quad \text{with} \quad (66)$$

$$\Gamma(Z) = \int e^{-t} t^{Z-1} dt, \text{ the gamma function.}$$

The root mean square deviation from the mean is  $\sigma = R_2/(Z+1)^{1/2}$ . The maximum of the curve is found at  $R = ZR_2/(Z+1)$ .

The three functions are plotted in [Figure 13-20](#).  $R_2$  is fixed at 200 Å. For the log-normal and the Schultz functions, the maximum of the curves are slightly smaller than  $R_2$ . The half-widths at  $G(R_2) \exp(-1/2)$  are related by:

$$\Delta R_2(\text{Gaussian}) = \sigma_0 R_2(\text{Log - Normal}) = R_2/(Z+1)^{1/2}(\text{Schultz}). \quad (67)$$

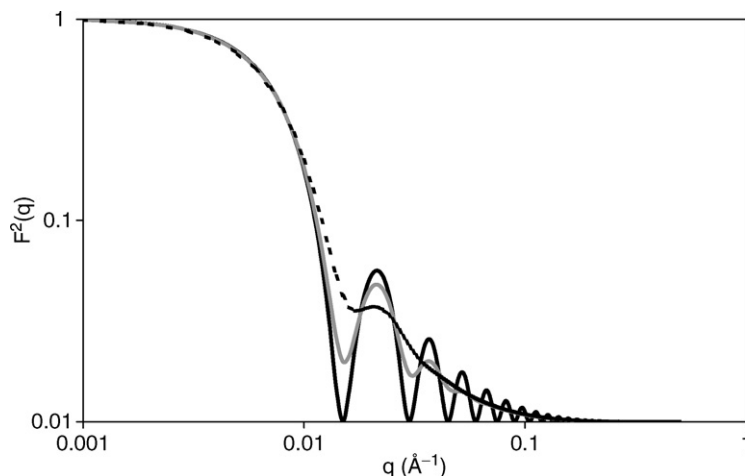
Finally, these three expressions yield very similar numerical values ([Figure 13-20](#)) and it is certainly not possible to distinguish them by a SANS experiment.

In the following, a log-normal law will be used to illustrate the effects of polydispersity. The effect of polydispersity on the form factor of a spherical shell of inner radius of 200 Å is illustrated in [Figure 13-21](#). It is clearly visible for  $\sigma_0 > 10\%$ . The oscillations vanish and the minimum of the first oscillation is shifted to higher  $q$  values.

## 6.5 Instrumental Resolution and Polydispersity

If one compares [Figure 13-17](#) and [Figure 13-21](#), the effects of polydispersity or instrument resolution are very similar. Indeed, mathematically, the smearing





■ Figure 13-21

Effect of the polydispersity on the ideal scattering of a monodisperse spherical shell,  $R_2 = 200 \text{ Å}$ . (—)  $\sigma_0 = 0$ ; (---)  $\sigma_0 = 10\%$ ; (....)  $\sigma_0 = 20\%$

equations (61) and (63) are similar. An experimental curve results from the smearing of the ideal intensity both by the resolution and the polydispersity functions:

$$I_{\text{exp}}(q_0, R_2) = \int_0^\infty R(q_0, q') \left[ \int_0^\infty K_c G(R_2, r, \Delta R_2) F^2(r, q) dr \right] dq' \quad (68)$$

As  $q$  and  $R_2$  are independent variables, (68) is also equal to:

$$I_{\text{exp}}(q_0, R_2) = \int_{R=0}^{R \rightarrow \infty} \int_{q \rightarrow -\infty}^{q \rightarrow +\infty} K_c R(q_0, q) G(R_2, r, \Delta R_2) F^2(r, q) dr dq \quad (69)$$

Remark: Taking a Gaussian law for the polydispersity, the total resolution function is symmetrical according to the variables  $q$  and  $r$ . Thus, the smearing effects due to  $\Delta r_0$  or  $\Delta q_0$  may be equivalent.

## 6.6 Conclusion

The contribution of the instrumental resolution to the scattering pattern is a general question. This knowledge is crucial for the data analysis because instrumental resolution and sample polydispersity have similar smearing effects on the SANS data. Smoothing of the form factor oscillations, broadening of Bragg peaks or of the maxima are observed. Plotting  $I(q)$  versus  $q$  in a log-log representation may show a decrease of the initial slope, due to a smearing by a large direct beam

may also be present [64]. As shown with simulation, 20% is the limiting value above which the smearing effect by the wavelength becomes drastic and yields to a real change in the scattered pattern.

The choice of collimation is a compromise between the flux and the resolution that has to be considered for each experiment.

## 6.7 Appendix: Definition of $\Delta\theta$ and $\Delta\lambda/\lambda$ ; Comparison between Triangle and Gaussian Functions

In the entire text, Gaussian functions are used to describe the wavelength and the angular distribution. We define here how the widths  $\Delta x_0$  of the Gaussian functions are calculated.  $\Delta\lambda/\lambda$  usually given is the FWHM which is different from  $\Delta x_0$

We recall that a Gaussian function centered on  $x_0$  of half width  $\Delta x_0$  at the value

$$G(x, x_0, \Delta x_0) = \frac{1}{\sqrt{2\pi}\Delta x_0} \exp(-1/2)$$

is given by:

$$G(x, x_0, \Delta x_0) = \frac{1}{\sqrt{2\pi}\Delta x_0} \exp\left(-\frac{(x - x_0)^2}{2\Delta x_0^2}\right). \quad (70)$$

The FWHM of a Gaussian is

$$\text{FWHM} = 2\Delta x_0 \sqrt{2 \ln 2}. \quad (71)$$

### 6.7.1 Wavelength Distribution

The wavelength distribution is ideally triangular but experiments show that Gaussian fits give reasonable results and improve the numerical treatment [65].  $\Delta\lambda/\lambda$  is deduced from the FWHM of the triangular function. It is usually between 5 and 20% with a neutron velocity selector, a value determined by time-of-flight measurements. Gaussian and triangular functions are compared in [Figure 13-22](#).

A triangular function of unit area, centered on  $\lambda_0$  of FWHM  $\lambda_0(\Delta\lambda/\lambda)$  is given by:

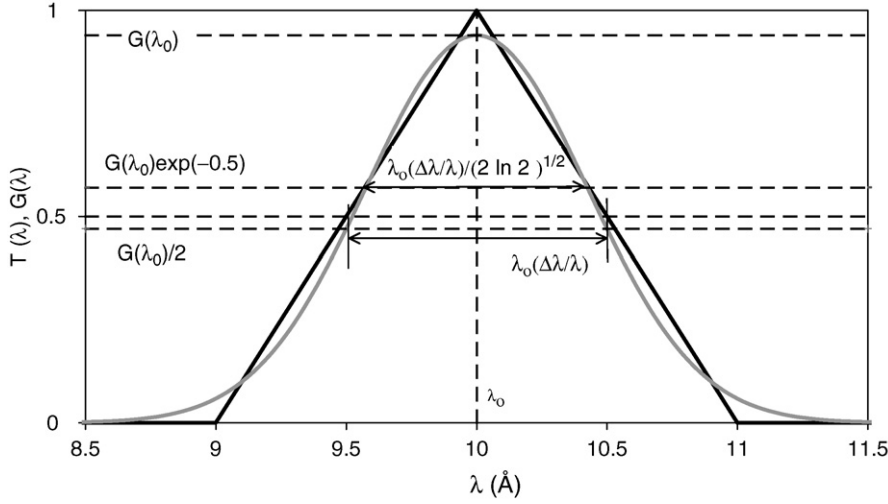


Figure 13-22

Comparison between triangular and Gaussian functions with the same areas used to represent the wavelength distribution

$$T(\lambda) = \frac{1}{[\lambda_0(\Delta\lambda/\lambda)]^2} \lambda + \frac{\lambda_0(1 - (\Delta\lambda/\lambda))}{[\lambda_0(\Delta\lambda/\lambda)]^2}; \quad \lambda \leq \lambda_0$$

$$T(\lambda) = \frac{-1}{[\lambda_0(\Delta\lambda/\lambda)]^2} \lambda + \frac{\lambda_0(1 + (\Delta\lambda/\lambda))}{[\lambda_0(\Delta\lambda/\lambda)]^2}; \quad \lambda \geq \lambda_0$$
(72)

The calculation uses a Gaussian function where the relevant parameter is  $\sigma_\lambda$ , the half width at the value  $\frac{1}{\sqrt{2\pi}\sigma_\lambda} \exp(-1/2)$ .

We replace the triangular function by a Gaussian one with the same FWHM. From (71), one deduces:

$$\sigma_\lambda = \frac{\lambda_0(\Delta\lambda/\lambda)}{2\sqrt{2\ln 2}}.$$
(73)

Thus, the relative wavelength spread introduces in (59) is:

$$(\delta\lambda/\lambda) = \frac{(\Delta\lambda/\lambda)}{2\sqrt{2\ln 2}}.$$
(74)

### 6.7.2 Angular Distribution

The angular distribution  $\Delta\theta$  is deduced from the width of the direct beam. For  $q = 0$   $\theta = 0$  and (58) is reduced to:

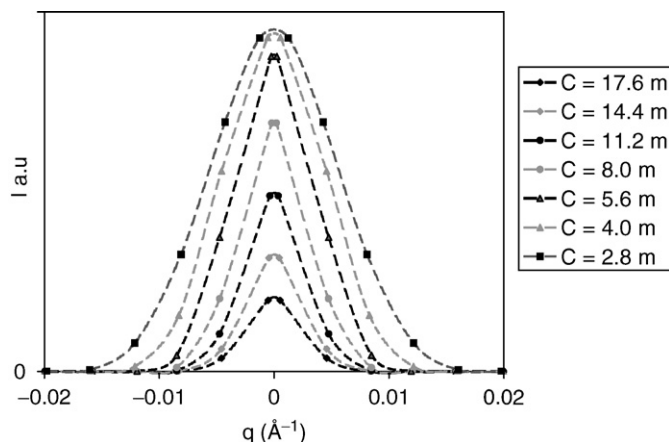


Figure 13-23

Shape and size of the direct beam of D22 at  $\lambda = 6 \text{ \AA}$  for the different possible collimation distances. Dotted lines are a guide for the eyes

$$\Delta q(0) = \frac{4\pi}{\lambda} \Delta \theta. \quad (75)$$

On D22, the measurements show that reasonable fits are obtained with a Gaussian function, even if deviation is observed in the tails. In these conditions  $\Delta q(0)$  is equivalent to  $\Delta x_0$  in (70) and one easily deduce  $\Delta \theta$  with (75).

Example of experimental direct beam shapes for  $\lambda = 6 \text{ \AA}$  at various collimation distances  $C$  are presented in Figure 13-23.

$\Delta \theta$  can also be calculated in a theoretical way from the geometry of the instrument. It is a function of: source diameter ( $S_1$ ), diameter of the aperture in front of the sample ( $S_2$ ), collimation ( $C$ ), and sample-to-detector ( $D$ ) distances. Details of calculations are given in [67, 68]. As a crude approximation,  $\Delta \theta$  can be estimated with:

$$\Delta \theta = S_1 / C. \quad (76)$$

## 7 Present Future and Perspective

### 7.1 Recent Developments

The new generation of SANS diffractometers like D22 at the ILL (Institut Laue Langevin, Grenoble) with very high flux at the sample position (up to  $10^8$  neutrons/s/cm<sup>2</sup>) combined with a large sensitive detector area permit very short acquisition times of the order of a few hundreds of milliseconds [72].

The development of new experiments is closely related to instrument improvement and development of new sophisticated sample environments. Great progress has been realized in the detector field and electronics as already presented in [Section 2](#). In the last few years, complex environments such as stopped-flow device, shear apparatus, extruder equipment, and flash light opened the possibility of new kind of investigations.

The last decade has seen the development of kinetics experiments. By rapid, one means acquisition of the order of hundred milliseconds in order to reach the early stages of formation of a sample. Real-time means a movie of the sample, just after a perturbation (dilution, pH jump, temperature change, application of a magnetic field, etc.). The knowledge of the early stage of sample formation can be crucial to understand and act on the equilibrium state. One crucial step with such experiments is to trigger the acquisition with the experimental setup to insure the reproducibility of the measurement. Small acquisition times require repeating several times the experiment and adding data to increase the statistics.

Real-time experiments carried out with the stopped-flow technique have allowed the study of intermediary or metastable states during the formation of vesicles [73–75], or to measure characteristic times for formation and growth of mesoporous materials [76].

In a recent experiment, the changes of conformation of the Photoactive Yellow Protein were followed during 1.053 s after illumination by a flash light [17]. The first acquisition time was only 50 ms, a time competitive with what is done on SAXS instruments on synchrotron sources. The analysis by IFT has shown an increase of the radius of gyration corresponding to an opening of the conformation just after illumination followed by a return to the equilibrium state within a second.

## 7.2 Future Developments

### 7.2.1 Interactive Instrument Control

The future of SANS experiments will require the development of new “intelligent” softwares that will be able not only to control the instrument and to set the configurations but also to pilot the acquisition. A major question, for example, is how to optimize the acquisition time by keeping good statistics. Future software will be able to calculate on line statistics and errors and to stop the acquisition when given conditions defined by the scientist (for example, a given number of neutrons) will be reached.

## 7.2.2 Lenses and Focusing

The limiting factors in neutron experiments are the flux, the smallest scattering vector ( $q_{\min}$ ), and the resolution, three parameters that can be linked and simultaneously improved if focusing devices would exist. The recent investigations consist in sets of biconcave lenses installed just before the sample [77]. Very encouraging results have been obtained as described by Choi et al. [78] with test experiments carried out on the 30-m SANS instrument at NIST [78]. The authors show the gain of flux, of minimum  $q$  and resolution after correction of chromatic aberration due to gravity. Nevertheless, some restrictions must be pointed out [79]. Mainly, such equipment decreases the instrument flexibility such as it is optimized for one wavelength and one sample-to-detector distance which must match the focusing point.

Sets of MgF Compound Refractive Lens (CRL) are available on D22 (obtained from PSI). Installed after the sample position they were used to magnify the sample. Example are given in [80] obtained with Al CRL.

## 7.2.3 Ultra Small-Angle Scattering (USANS)

At very low  $q$  SANS experiments meet the limits of light scattering experiments. Micro-size particles can be analyzed by techniques like electronic microscopy, AFM, light scattering or USAXS but in some cases these techniques are not applicable (opaque sample for SALS, low contrast, etc.). USANS offers the possibility to investigate very large structures. Worm-like micelles, microemulsions, colloidal crystals, porous material as found in cement or rocks are possible applications in USANS.

USANS instruments can cover a  $q$ -range from  $2 \cdot 10^{-4}$  to  $5 \cdot 10^{-3} \text{ \AA}^{-1}$ . They operate mainly according two principles. The Bonse–Hart setup consists in two channel-cut perfect crystals mounted in parallel, one is the monochromator, the second one is the analyzer and the sample is positioned in between. The  $q$ -dependence of the scattered intensity is measured by rocking the crystals [78]. Bonse–Hart-type instruments exist on PCD at the NIST (USA), on S18 at the ILL (France), on ECHO at SINQ (Switzerland), on KWS-3 in the FZ-Jülich (Germany), and will also be built in Jaeri the new spallation source in Japan.

The second possible setup is a pinhole geometry, where the beam is collimated in the two directions by a series of small diaphragms or slits. This geometry has been selected at the LLB (France) for the instrument “TPA” in commissioning at the date of this review [83] [84].

One main limiting factor in USANS experiments is the low flux at the sample position.

Nevertheless the new high flux reactors and spallation sources render the experiments possible. The use of multiple small beams further focused at the sample position is an efficient way to increase the flux.

## 7.2.4 Polarization and SANS

Some SANS spectrometers<sup>1</sup> offer now a polarization option opening new possible fields of research. The polarization has a strong influence on the contrast between nuclear and magnetic scattering contribution. The incident polarized beam is produced by a supermirror. Polarization alone can be used as a way to vary the contrast of the sample. The principle of a “polarization plus analysis” experiment consists in applying a magnetic field to the sample and to analyze the spin states before and after the scattering. Complementary to conventional SANS, additional information magnetization profiles in samples are obtained. Recent outcomes on ferrofluids are described in [16].

Another application comes from the large spin-dependent scattering length from  $^1\text{H}$ . Consequently, polarized SANS can find strong application in soft condensed matter and biology where hydrogen is a main component. Contrast variation can be done once again using hydrogen  $^1\text{H}$  and deuterium  $^2\text{H}$  which exhibit strong differences in spin-dependence [82].

Nanotechnologies using magnetism and new biotechnologies will certainly benefit from polarized SANS, opening new approaches for the sample characterization.

## 7.3 General Conclusion

SANS is a powerful technique to analyze the size, the shape, the intra- and interstructures of complex systems with typical size ranging from a few nanometres down to tenths of a micrometer. The lowest flux and the larger beam size compared to X-ray source is balanced by the unique feature of isotopic substitution which has been of particular importance in the understanding of biological systems.

In comparison with light or X-ray scattering, small-angle neutron scattering is a relatively recent technique, still in evolution. Technical progresses are also closely linked to electronics improvements. Progress in computing permits more

---

<sup>1</sup> PAPOL, LLB, France; SANSPOL, HMI, Germany; SANS-I at SINQ, Switzerland, NG3 30m at NIST, United States

and more accurate fittings with numerical resolution of nonlinear equations involved in theoretical models.

SALS, SAXS, and SANS techniques are not in competition but really complementary. Moreover microscopy techniques (in the real space) are often carried out in parallel to validate the models deduced from scattering experiments. Reference [41] illustrates nicely the complementarities of freeze-fracture electron microscopy and SANS.

The increasing number of proposals submitted per year demonstrates the relevance of this technique. The future developments and the broad field of research investigated insure a bright future for SANS experiments.

## Acknowledgements

I would warmly thank Dr. S King and Dr R. Heenan (ISIS), for the documents supplied on LOQ. I am grateful to P. Van Esch (ILL, Grenoble) for the technical explanations on detectors. I am grateful to Ron Ghosh (Institut Laue Langevin) for discussion on instrument resolution. I would like to thank Bruno Demé for helpful discussions in perspective and application for USANS instruments. Thanks to C. Dewhurst for the manuscript reading and comments on data analysis. I thank R. May for the training on D22 at the ILL and all fruitful discussions.

## References

1. Guinier, A. (1939) *Ann. Phys. Paris.*, **12**, 161–237.
2. Guinier, A., Fournet, G. 1955 *Small Angle Scattering of X-Rays*. Wiley, New York.
3. Stuhmann, H.B. (1974) Neutron Small-angle scattering of biological macromolecules in solution. *J. Appl. Cryst.*, **7**, 173–178.
4. Stuhmann, H.B. and Duee, E.D. (1975) The determination of the scattering density distribution of polydisperse solutions by contrast variation: a neutron scattering study of ferritin. *J. Appl. Cryst.*, **8**, 538–542.
5. Ibel, K. and Stuhmann, H.B. (1975) *J. Mol. Biol.*, **93**, 255–265.
6. <http://www.ill.eu/lss/more/world-directory-of-sans-instruments/> and [http://www.isis.rl.ac.uk/LargeScale/LOQ/other/World\\_Directory\\_of\\_SANS\\_Instruments.htm](http://www.isis.rl.ac.uk/LargeScale/LOQ/other/World_Directory_of_SANS_Instruments.htm).
7. Glinka, C.J., Barker, J.G., Hammouda, B., Krueger, S., Moyer, J.J., and Orts, W.J. (1998) The 30 m small angle neutron scattering experiments at the national institute of standards and technology. *J. Appl. Cryst.*, **31**, 430–445.
8. Heenan, R.K., Penfold, J., King, S.M. (1997) SANS at pulsed neutron sources: present and future prospects. *J. Appl. Cryst.*, **30**, 1140–1147 (<http://www.isis.rl.ac.uk/largescale/loq/loq.htm>).



9. Knoll, G.F. and Wihley J.(1989) Position-sensitive detection of thermal neutrons. In Convert, P. and Forsyth, J.B. (ed.), *Radiation Detection and Measurement*. Academic Press, New York.
10. Knoll, G.F. 1989. *Radiation Detection and Measurement*, Chap. 7, 2nd ed. Wiley, New York; P. Lindner, Dead time of the BF3 detector at D11, ILL Technical report, ILL98/LI 12 T (1998).
11. Van Esc, P., Gahl, T., Guérard, B. (2004) Design criteria for electronics for resistive charge division in thermal neutron detection. *Nucl. Instr. Meth. Phys., Res. A*, **526**, 493–500.
12. Van Esch, P. and Millier, F. (2003) Optimal lookup table construction with respect to efficiency flatness. *Rev. Sci. Instrum.*, **74**, 5058–5061.
13. Scherm, R. and Fak, B. (1993). Neutron and synchrotron radiation for condensed matter studies. In Baruchel, J. Hodeau, J.L., Lehmann, M.S., Regnard, J.R., and Schlenker C. (eds.), *Theory, instruments and methods*. Les Editions de physique, Vol 1, Chap. 5. Springer, Berlin.
14. May, R., Hendriks, J., and Crielaard, W. (2005) Real-time neutron scattering investigations of biological signal transduction dynamics. In *Proceedings of the International Symposium on Research Reactor and Neutron Science*, Daejeon, Korea, pp 777–781.
15. Bent, J., Hutchings, L.R., Richards, R.W., Cough, T., Spares, R., Coates, P.D., Grillo, I., Harlen, O.G., Read, D.J., Graham, R.S., Likhtman, A.E., Groves, D.J., and Nicholson, T.M (2003) Neutron -mapping polymer flow: scattering flow visualization and molecular theory. *T.C.B. McLeish Sci.*, **301**, 1691–1695 (abstract).
16. Heinemann, A., Wiedenmann, A. (2005) Insight into the formation of partially ordered structures in Co-based ferrofluids. *J. Magn. Magn. Mater.*, **289**, 149–151.
17. Jacrot, B. and Zaccai, G. (1981) Determination of molecular weight by neutron scattering. *Biopolymers*, **20**, 2413–2426.
18. Lindner, P. (2000) Water calibration at D11 verified with polymer samples. *J. Appl. Crystallogr.*, **33**, 807–811.
19. Gosh, R.E, Egelhaaf, S.U., and Rennie, A.R. (1998) A computing guide for Small-Angle Scattering Experiments; ILL report ILL98GH14T. GRASP for Graphical Reduction and analysis SANS program for Matlab™ by C. Dewhurst ([http://www.ill.eu/sites/grasp/grasp\\_main.html](http://www.ill.eu/sites/grasp/grasp_main.html)).
20. Sears, V.F. (1992) Neutron scattering lengths and crossed sections. *Neutron News*, **3**, 26–37.
21. Schelten, J. and Schmatz, W. (1980) Multiple scattering treatment for small-angle scattering problems. *J. Appl. Crystallogr.*, **13**, 385–390; Goyal, P.S., King, J.S., and Summerfield, G.C. (1983) Multiple scattering in small-angle neutron scattering measurements on polymers. *Polymer*, **24**, 131–134; Berk, N.F. and Hardman-Rhyne, K.A. (1988) Analysis of SAS data dominated by multiple scattering. *J. Appl. Crystallogr.*, **21**, 645–651.
22. Lal, J., Widmaier, J.M., Bastide, J., and Boué, F. (1994) Determination of an interpenetrating network structure by small angle neutron scattering. *Macromolecules*, **27**, 6443–6451.
23. Morfin, I., Ehrburger-Dolle, F., Grillo, I., Livet, F., and Bley, F. (2006) ASAXS, SAXS and SANS investigations of vulcanized elastomers filled with carbon black. Part 6, 445–452.
24. Brûlet, A., Lairez, D., Lapp, A., Cotton, J.P. (2007) Improvement of data treatment in small-angle neutron scattering *J Appl Cryst.* **40**, 165–177.
25. Silas, J.A. and Kaler, E.W. (2003). Effect of multiple scattering from bicontinuous microemulsions. *J. Colloid Interface Sci.*, **257**, 291–298.
26. Glatter, O. and Kratky, O. 1982 *Small Angle X-Ray Scattering*. Academic Press, London.
27. Boué, F., Cotton, J.P., Lapp, A., and Jannink, G. (1994) A direct measurement of the polyion conformation in aqueous solutions at different temperatures. Small angle neutron scattering of PSSNa using

- zero average and full contrast. *J. Chem. Phys.*, **101**, 2562–2568; Brûlet, A., Boué, F., Cotton, J.P. (1996) About the experimental determination of the persistence length of wormlike chains of polystyrene. *J. Phys. II France*, **6**, 885–891; Spitéri, M.N., Boué, F., Lapp, A., and Cotton, J.P. (1996) Persistence length for a PSSNA Polyion in semidilute solution as a function of the ionic strength. *Phys. Rev. Lett.*, **77**, 5218–5220.
28. Morfin, I., Lindner, P., and Boué, F. (2004) Shear-induced concentration fluctuations and form factor changes in polymer solution in the good-solvent regime. *Eur. Phys. J. E.*, **15**, 41–45.
29. Oberdisse, J. (2007) Current Opinion in Colloid and Interface Science. Adsorption grafting on colloidal interfaces studied by scattering techniques. **12**, 3–8.
30. Boué, F., Cousin, F., Gummel, J., Oberdisse, J., Carrot, G., El Harrack, A. (2007) Small angle scattering from soft matter – application to complex mixed systems. *C.R. Phys* **8**, 821–844.
31. Balnois, E., Durand-Vidal, S., and Levitz, P. (2003) Probing the morphology of Laponite clay colloids by atomic force microscopy. *Langmuir*, **19**, 6633–6637.
32. Mourchid, A., Delville, A., Lambard, J., Lécolier, E., and Levitz, P. (1995) Phase diagram of colloidal dispersions of anisotropic charged particles: equilibrium properties, structure and rheology of laponite suspensions. *Langmuir*, **11**, 1942–1950.
33. Grillo, I. (personal communication).
34. Bates, F.S., Wignall, G.D., and Koehler, W.C. (1985) Critical behavior of binary liquid mixtures of deuterated and protonated polymer. *Phys. Rev. Lett.*, **55**, 2425.
35. Arleth, L. and Pedersen, J.S. (2000) Scattering vector dependence of the small-angle scattering from mixtures of hydrogenated and deuterated organic solvents. *J. Appl. Crystallogr.*, **33**, 650–652.
36. Jacrot, J. (1976) The study of biological structures by neutron scattering from solution. *Rep. Prog. Phys.*, **39**, 911–953.
37. Pedersen J. (1997) Analysis of small-angle scattering data from colloids and polymer solutions: modeling and least-squares fitting. *Adv. Colloid Interface Sci.*, **70**, 171–210.
38. Rayleigh, L. (1911) The Incidence of Light upon a Transparent Sphere of Dimensions Comparable with the Wave-Length. *Proc. Royal. Soc. London. Ser. A.*, **84**, 25–38.
39. Dingenouts, N., Selenmeyer, S., Deike, I., Roseneldt, S., Ballauf, M., Lindner, P., and Narayanan, T. (2001) Analysis of thermosensitive core-shell colloids by small-angle neutron scattering including contrast variation. *Phys. Chem. Chem. Phys.*, **3**, 1169–1174.
40. Sommer, C., Pedersen, J.S., and Garamus, V.M. (2005) Structure and interaction of block copolymer micelles of Brij 700 studied by combining small-angle X-ray and neutron scattering. *Langmuir*, **21**, 2137–2149.
41. Bumajdad, A., Eastoe, J., Nave, S., Steytler, D.C., Heenan, R.K., and Grillo, I. (2003) Compositions of mixed surfactant layers in microemulsions determined by SANS. *Langmuir*, **19**, 2560–2567.
42. Fournet, G. (1951) *Bull. Soc. Fr. Minér. Crist.*, **74**, 39–113.
43. Eastoe, J., Rogueda, P., Shariatmadai, D., and Heenan, R. (1996) Micelles of asymmetric chain catanionic surfactants. *Colloids surf. A Physicochem. Eng. Asp.*, **117**, 215–225.
44. Zemb, T., Dubois, M., Demé, B., and Gulik-Krzywicki, T. (1999) Self-assembly of flat nanodiscs in salt-free catanionic surfactant solutions. *Science*, **283**, 816–819.
45. Coulombeau, H., Testard, F., Zemb, T., and Larpent, C. (2004) Effect of recognized and unrecognized salt on the self-assembly of new thermosensitive metal-chelating surfactants. *Langmuir*, **20**, 4840–4850.
46. Simmons, B., Agarwal, V., McPherson, G., John, V., and Bose, A. (2002) Small angle neutron scattering study of mixed AOT + lecithin reverse micelles. *Langmuir*, **18**, 8345–8349.
47. Jung, M., Robinson, B.H., Steytler, D.C., German, A.L., and Heenan, R.K. (2002) Polymerization of styrene in DODAB vesicles: a small-angle neutron scattering study. *Langmuir*, **18**, 2873–2879.

48. Caillé, A. (1972) X-ray scattering by smectic-A crystals. *C. R. Hebd. Acad. Sci. Paris B.*, **274**, 891–893.
49. Nallet, F., Laversanne, R., and Roux, D. (1993) Modelling X-ray or neutron scattering spectra of lyotropic lamellar phases. Interplay between form and structure factors. *J Phys. II*, **3**, 487–502.
50. Grillo, I. (2003) Small angle neutron scattering of a world-wide known emulsion: Le Pastis *Colloids surf. A Physicochem. Eng. Asp.*, **225**, 153–160.
51. Marchal, D., Bourdillon, C., and Demé Small-Angle, B. (2003) Neutron scattering by highly oriented hybrid bilayer membranes confined in anisotropic porous alumine. *Langmuir*, **26**, 8313–8320.
52. Demé, B. and Zemb, T. (2000) Measurement of sugar depletion from uncharged lamellar phases by SANS contrast variation. *J. Appl. Cryst.*, **33**, 569–573.
53. Kanaya, T., Ohkura, M., Takeshita, H., Kaji, K., Furusaka, M., Yamaoka, H., and Wignall, G.D. (1995) Gelation process of poly(vinyl alcohol) as studied by small-angle neutron and light scattering. *Macromolecules*, **28**, 3168. The Netherlands, Amsterdam.
54. Steytler, D.C., Dowding, P.J., Robinson, B.H., Hague, J.D., Rennie, J.H.S., Leng, C.A., Eastoe, J., and Heenan R.K. (1998) Characterization of water-in-oil microemulsions formed in silicone oils. *Langmuir*, **14** 3517–3523.
55. Auvray, L. and Auroy, P. (1991) Neutron, X-Ray and light scattering: introduction to an investigative tool for colloidal and polymeric systems. In Lindner, P. and Zemb, T. (eds.), North Holland delta series. III. Scattering by interfaces: variation on Porod's law. The Netherlands, North Holland delta series, Amsterdam.
56. Glatter, O. (1977) Data evaluation in small-angle scattering, calculation of radial electron density distribution by means of indirect fourier transformation. *Acta Phys. Austriaca*, **47**, 83–102; Glatter, O. (1977) New method for evaluation of small angle scattering data. *J. Appl. Crystallogr.*, **10**, 415–421; Glatter, O. (1980) Determination of particle size distribution functions from small-angle scattering by means of the indirect transformation method. *J. Appl. Crystallogr.*, **13**, 7–11.
57. Lindner, P., and Zemb, T. (eds.) (2002) Neutron, X-rays and light: scattering methods applied to soft condensed matter, chaps. 4 and 5. Elsevier. The Netherlands, Amsterdam.
58. Weyerich, B., Brunner-Popela, J., and Glatter, O. (1999) Small-angle scattering of interacting particles. II. Generalized indirect Fourier transformation under consideration of the effective structure factor for polydisperse systems. *J. Appl. Crystallogr.*, **32**, 197–209.
59. Svergun, D.I. and Koch, M.H.J., (2003) Small-angle scattering studies of biological macromolecules in solution. *Rep. Prog. Phys.*, **66**, 1735–1782.
60. Lindner, P. and Zemb, T. (eds.) (2002) Neutron, X-rays and Light: Scattering Methods Applied to Soft Condensed Matter, chapters 14. Elsevier.
61. Percus, J.K and Yevick, G.J. (1958) Analysis of classical mechanics by means of collective coordinates. *Phys Rev.*, **1**, 1–13.
62. Hayter, J.B. and Penfold, J. (1981) An analytic structure factor for macroion solutions. *Mol. Phys.*, **42**, 109–118.
63. Hansen, J.P. and Hayter, J.B. (1982) A rescaled MSA structure factor for dilute charged colloidal dispersions. *Mol. Phys.*, **46**, 651–656.
64. Schmatz, W., Springer, T., Schelten, J., and Ibel, K. (1974) Neutron small-angle scattering - Experimental techniques and applications. *J. Appl. Cryst.*, **7**, 96–116; Wignall, G.D., Christen, D.K., and Ramakrishnan V. (1988) Instrumental resolution affects in small-angle neutron scattering *J. Appl. Cryst.*, **21**, 438–451; Milder, D.F.R. (1990) Design optimization of a small-angle neutron scattering spectrometer. *Nucl. Instrum. Methods Phys. Res. A*, **290**, 259–262.
65. Pedersen, J.S., Posselt, D., and Mortensen, K. (1990) Analytical treatment of the resolution function for small-angle scattering. *J. Appl. Crystallogr.*, **23**, 321–333.
66. Mildner, D.F.R., Carpenter, J.M., and Worcester, D.L. (1986) Measurement and calculation of resolution of time-of-flight

- small-angle neutron scattering *J. Appl. Crystallogr.*, **19**, 311–319.
67. Né, F., Grillo, I., Taché, O., and Zemb, T.H. (2000) De l'intensité brute à l'intensité absolue, calibration d'une camera Guinier-Mering. *J. Phys. IV*, **10**, 403–413.
68. Huang, T.C., Toraya, H., Blanton, T.N., and Wu, Y (1993) *J. Appl. Crystallogr.*, **26**, 180–184.
69. Grillo, I. (2001) ILL technical Report ILL01GR08T, Effect of instrumental resolution and polydispersity on ideal form factor in Small Angle Neutron Scattering.
70. Mildner, B.F.R. and Carpenter, J.M. (1984) Optimization of the experimental resolution for small-angle scattering. *J. Appl. Crystallogr.*, **17**, 249–256.
71. Lairez, D. (1999) Résolution d'un spectromètre de diffusion de neutrons aux petits angles. *J. Phys. IV France*, **9**, 67–81.
72. <http://www.ill.eu/dzz/documentation/>.
73. Egelhaaf, S.U., Olsson, U., and Schurtenberger, P. (2000) Time resolved SANS for surfactant phase transitions. *Physica B*, **276–278**, 326–329.
74. Grillo, I., Kats, E.I., and Muratov, A.R. (2003) Formation and growth of anionic vesicles followed by small-angle neutron scattering. *Langmuir*, **19**, 4573–4581.
75. Gradzielski, M., Grillo, I., and Narayanan, T. (2004) Dynamics of structural transitions in amphiphilic systems monitored by scattering techniques. *Prog. Colloid. Polym. Sci.*, **129**, 32–39.
76. Né, F., Testard, F., Zemb, T., et al. (2003) How does ZrO<sub>2</sub>/surfactant mesophase nucleate? Formation mechanism. *Langmuir*, **19**, 8503–8510.
77. Williams, R.E. and Michael Rowe J. (2002) Developments in neutron beam devices and in advanced cold source for the NIST research reactor. *Physica B*, **311**, 117–122.
78. Choi, S.M., Barker, J.G., Glinka, C.J., Cheng, Y.T., and Gammel, P.L. (2000) Focusing cold neutrons with multiple biconcave lenses for small-angle neutron scattering. *J. Appl. Crystallogr.*, **33**, 793–796.
79. Littrell, K.C. (2004) A comparison of different methods for improving flux and resolution on SANS instrument. *Nucl. Instrum. Methods Phys. Res. A*, **529**, 22–27.
80. Dewhurst, C.D., Anderson, I., and Beguiristain, R. (2001) ILL Annual Report. In Cicognani, G. and Vettier, C. (ed.), *Imaging with a Neutron Lens*.
81. Bonse, U. and Hart, M. Small-Angle X-Ray Scattering. In Brumberger, H. (ed.), Gordon and Breach, New York, pp 121.
82. Stuhmann, H.B., Van der Brandt, B., Hautle, P., Konter, J.A., Ninikoski, T.O., Schmitt, M., Willumeit, R. Zhao, J., and Mango, S. (1997) Polarized neutron scattering from polarized nuclei near paramagnetic centres. *J. Appl. Crystallogr.*, **30**, 839–843.
83. Désert, S., Thevenot, J., Oberdisse, A., Brûlet, J. (2007) The new very-small-angle neutron scattering spectrometer at Laboratoire Leon Brillouin. *J. Appl. Cryst.*, **40**, S471–S473.
84. Brûlet, A., Thevenot, V., Lairez, D., Lecommandoux, S., Agut, W., Armes, S.P., Du, L.Z., Désert, S. (2008) Toward a new lower limit for the minimum scattering vector on the very small angle neutron scattering spectrometer at Laboratoire Leon Brillouin. *J. Appl. Cryst.*, **41**, 161–166.

Soft-Matter Characterization

Borsali, R.; Pecora, R. (Eds.)

2008, LXXII, 1452 p. Print + eReference., Hardcover

ISBN: 978-1-4020-8290-0